Res Chem Intermed (2014) 40:2737–2771
DOI 10.1007/s11164-013-1126-z

Review of the synthesis, characterization, and properties of $LaAlO_3$ phosphors

Jagjeet Kaur · Deepti Singh · Vikas Dubey · N. S. Suryanarayana · Yogita Parganiha · Pooja Jha

Received: 5 January 2013 / Accepted: 14 February 2013 / Published online: 23 March 2013

Abstract In this review different methods of preparing lanthanum aluminate ($LaAlO_3$) phosphors are discussed. The molten salt method, the combustion method, the sucrose method, and the coprecipitation technique are the best methods for preparing $LaAlO_3$ phosphors with small particle size and high surface area by low-temperature synthesis. $LaAlO_3$ usually has a rhombohedral structure. It has good dielectric properties and, hence, is regarded as an attractive alternative to SiO_2 in microelectronic devices. $LaAlO_3$ phosphors have excellent chemical and thermal stability, mechanical durability, and exploitable optical and electronic properties, leading to a wide range of potential applications. $LaAlO_3$ phosphors doped with rare-earth ions have luminescence properties and can, hence, be used in optical display systems.

Keywords Synthesis · Characterization · Dielectric study · $LaAlO_3$ phosphors

Introduction

Lanthanum aluminate ($LaAlO_3$) with a perovskite-type structure has, because of its properties, attracted much attention in recent years for many applications. Indeed, the material has good thermal stability with a high melting point, 2,180 °C, which can minimize interfacial dislocations [1]. Traditionally, $LaAlO_3$ has been prepared by conventional solid-state reaction of Al_2O_3 and La_2O_3 in the temperature range 1,500–1,700 °C [2, 3]. But this typical method suffers from many inherent

---

J. Kaur · D. Singh · V. Dubey (✉) · N. S. Suryanarayana · Y. Parganiha · P. Jha
Department of Physics, Government V.Y.T. PG. Autonomous College, Durg 491001,
Chhattisgarh, India
e-mail: jsvikasdubey@gmail.com

D. Singh
e-mail: deepti27.singh@gmail.com

shortcomings, for example high-temperature heat treatment, which has a detrimental effect on grain size, limited chemical homogeneity, and low sintering temperature.

Several low-temperature (750–900 °C) methods are used to prepare finer, more homogeneous powders of $LaAlO_3$; examples include the poly(vinyl alcohol) (PVA) with metal nitrate synthesis [4], sol–gel processes [5–7], the EDTA gel route [8, 9], co-precipitation methods [10, 11], pyrolysis using triethanolamine (TEA) [12], and combustion synthesis with urea as fuel [13, 14].

Review of the literature

Adak et al. reported preparation of pure $LaAlO_3$ powders by evaporation of PVA added to a mixed metal nitrate solution. Precursor powders and calcined powders were characterized by differential thermal analysis (DTA), thermogravimetric analysis (TGA), X-ray powder diffraction (XRD), and infrared (IR) spectroscopy. The crystallite size ranged between 10 and 20 nm. The dielectric properties of the material were also measured [4].

Taspinar et al. reported that a promising candidate for ferroelectric substrate materials, lanthanum monoaluminate ($LaAlO_3$), could be successfully synthesized by two separate chemical powder preparation techniques: homogeneous precipitation from aqueous solutions containing urea (CH_4N_2O) in the presence of nitrate salts, and self-propagating combustion synthesis from aqueous solutions containing CH_4N_2O and the nitrate salts of lanthanum and aluminium. The submicrometer, spherical-like particles of the precursors were completely converted to pure $LaAlO_3$ at 850 °C by homogeneous precipitation; the conversion temperature was observed to be 750 °C, the lowest ever reported for powder synthesis of a pure $LaAlO_3$ phase. The materials were characterized by powder XRD, simultaneous TGA and DTA, scanning electron microscopy (SEM), and energy-dispersive X-ray spectroscopy. Structure refinement by Rietveld analysis showed that $LaAlO_3$ was isostructural with $BaTbO_3$ and had the space group R-3C, in contrast with the R-3M space group previously assumed for this phase. The atomic positions in the structure of $LaAlO_3$ were refined and presented for the first time in this space group [15].

Jacobs et al. used molecular dynamics simulations to study the bulk and (100) surface of $LaA1O_3$. Bulk and surface structures and vibrational spectra are reported. AlO and LaO surface termination were both studied. LaO termination was clearly more stable than AlO termination [16].

Kakihana et al. reported synthesis of $LaAlO_3$ powders with large surface areas by the polymerized complex technique based on in-situ polyesterification between citric acid (CA) and ethylene glycol (EG). Heating of a mixed solution of CA, EG, and the nitrates of lanthanum and aluminium at 130 °C gave a brown transparent gel without any precipitation. The gel was preheated at 350 °C to give a black powdery mass, which was subsequently used as a precursor for $LaAlO_3$. Formation of pure perovskite $LaAlO_3$ occurred when the precursor was heat treated in a furnace set at 700 °C for 8 h or at 750 °C for 2 h. No XRD evidence of the presence of crystalline impurities was obtained. The $LaAlO_3$ powder prepared by the polymerized complex method had an very large surface area, in the range 13–16 $m^2 g^{-1}$, compared with

0.3 m^2 g^{-1} for the conventional solid-state reaction powder of the same compound [17].

Spinicci et al. investigated methane coupling at 600–750 °C over $LaAlO_3$, $La_{1-x}M_xAlO_3$ (M = Na, K, Ca, Ba, $x = 0.1$) and $LaAl_{1-x}M_xO_3$ (M = Li, Mg, $x = 0.1$) perovskite-type catalysts, prepared by calcining the citrate precursors at 800 °C for 5 h. Introduction of the alkali and alkaline earth metals produces oxygen vacancies and increases the bond strength of both lattice and surface oxygen species. Substitution of Al^{3+} with Li^+ and Mg^{2+} increases both catalytic activity and selectivity for C_2 hydrocarbons in comparison with unsubstituted $LaAlO_3$ perovskite. Diffusional control is suggested for oxidation to carbon oxides, whereas methane coupling should occur under kinetic control. The overall process involves a complex series of reactions. The results were rationalized on the basis of the structural properties of the catalysts and their adsorptive behavior towards oxygen, investigated by means of temperature-programmed desorption [18].

Hayward et al. used high-resolution X-ray rocking diffraction to measure the spontaneous strain associated with the cubic–rhombohedral phase transition in $LaAlO_3$ in the range $10 \leq T \leq 750$ K. The results were consistent with a second-order Landau-like model at high temperatures, with $T_C = 834(2)$ K. At lower temperatures, the strain data display order parameter saturation, related to quantum saturation of the phonon modes. Comparison of the saturation temperature for the spontaneous strain ($\theta_S = 95$ K) with the saturation temperatures for independent measurements of the rotation ($\theta_S = 260$ K) and distortion ($\theta_S = 150$ K) of the AlO_6 octahedra reveals that the phase transition consists of two coupled processes, and that coupling does not have the same effect in the classical and quantum saturation limits [19].

Deren et al. reported the absorption, time-resolved emission spectra, and decay times of $LaAlO_3$:Eu^{3+}. It was found that emission by $LaAlO_3$:Eu^{3+} crystals is very efficient. Observed peaks were assigned to $^5D_{3,2,1,0} \rightarrow {}^7F_J$ transitions. The strongest emission observed was that from the $^5D_0$ level to the $^7F_{1,2,4}$ levels. Decay time of the $^5D_0$ emission was 2.44 ms at 4.5 K, with weak dependence on temperature. Decay times of the $^5D_1$ and $^5D_2$ levels were short, and highly dependent on temperature. Energy levels of Eu^{3+} in $LaAlO_3$ were assigned [20].

Xiang et al. reported epitaxial growth of $LaAlO_3$ films on Si (100) substrates by inserting an SrO or $SrTiO_3$ buffer layer by use of a computer-controlled laser molecular beam epitaxy system. Structural characterization indicated that the $LaAlO_3$ films were two-dimensional (2D) layer-by-layer growth. Atomic force microscopy (AFM) observations revealed that the surfaces of the epitaxial $LaAlO_3$ films were atomically smooth. The crystallinity of the $LaAlO_3$ films determined by XRD and high-resolution transmission electron microscopy (HRTEM) was a single-crystalline structure. After annealing at 1,050 °C in N_2 for 5 min, the crystallinity of the $LaAlO_3$ film clearly improved. Successful $LaAlO_3$–SrO–Si and $LaAlO_3$–$SrTiO_3$–Si epitaxial growth suggested the possibility of development of 3D heterostructures on Si in a new generation of microelectronics devices [21].

Deren et al. reported measurement of absorption, emission, and emission decay times of Ho^{3+} ions embedded in an $LaAlO_3$ single crystal. The experimental results were analyzed on the basis of Judd–Ofelt (J–O) theory. Energy levels, oscillator strengths, and probabilities of radiative transition were determined. The results indicated non-radiative transitions occurred because of cross-relaxation down and up-conversion processes [22].

Fidancev et al. reported measurement of the absorption and emission of Er^{3+}-doped $LaAlO_3$ crystals at room and low temperature (10 K). Preliminary crystal-field calculations were performed on the basis of these experimental results. The energy levels of Er^{3+} in $LaAlO_3$ were well reproduced [23].

Busani et al. reported use of grazing incidence X-ray reflectivity measurements to determine the density of sputter-deposited $LaAlO_3$ and anodized LaAl films. The results, with refractive index and dielectric constant measurements, resulted in a coherent explanation of the low dielectric constant of the amorphous films (~ 13) compared with the single-crystal value (~ 26). The importance of the dependence of molecular volume on electronic and vibrational molecular polarizabilities was emphasized [24].

Chang et al. reported details of a process for preparation of an Eu^{2+}-activated long-lasting $Sr_4Al_{14}O_{25}$ nano-sized phosphor by the precipitation method. SEM, simultaneous differential scanning calorimetry (DSC)–TGA, XRD, photoluminescence spectroscopy (PLS), and thermal luminescence spectroscopy were used to characterize the phosphor. Nano-scale $SrAl_2O_4$:$Eu^{2+}Dy^{3+}$ and $Sr_4Al_{14}O_{25}$:$Eu^{2+}Dy^{3+}$ phosphors were obtained by calcining the precipitated precursors at 1,200 and 1,300 °C, respectively. Both the low-temperature product $SrAl_2O_4$:$Eu^{2+}Dy^{3+}$ and the high-temperature product $Sr_4Al_{14}O_{25}$:$Eu^{2+}Dy^{3+}$ emitted photoluminescence (PL) on ultraviolet (UV) illumination; emission peaks were at 480 and 505 nm, respectively. Compared with the emission spectrum of the powder obtained by use of the conventional method, a blue shift was observed for the nano-sized powders, because of the decrease in grain size. These two phosphors had a long-persistence afterglow; that of the $Sr_4Al_{14}O_{25}$:$Eu^{2+}Dy^{3+}$ phosphor was better than that of the $SrAl_2O_4$:$Eu^{2+}Dy^{3+}$ phosphor, because of a deeper trap level and a higher trap concentration in the host material [25].

Hreniak et al. reported the preparation, morphology, and structural properties of Eu^{3+}-doped $LaAlO_3$ nano-crystallites prepared by Pechini's (Pe) method. The effects of annealing temperature and Eu-ion content on the process of formation of the nano-crystallites were investigated. Preliminary studies were conducted on the effect of $LaAlO_3$ nano-crystallite size on the luminescence properties of the Eu ions. Time-resolved luminescence spectra and decay times were recorded for powders of different grain size. It was found that nano-crystallite size affected radiative relaxation of Eu^{3+} luminescence [26].

Deren et al. reported observation of anti-Stokes intense green emission after direct excitation of the $^5F_5$ level of Ho^{3+} in $LaAlO_3$. Up-conversion was observed, because of strong excited state absorption (ESA) in which two intermediate levels the $^5I_7$ and the $^5I_6$, were involved. Power dependence of the anti-Stokes emission depends on excitation wavelengths. The mechanism of the ESA was discussed in detail [27].

Ishigaki et al. used a novel "melt synthesis technique", rather than conventional solid-state reaction techniques, to synthesize a variety of perovskite ABO_3-type compounds and their solid solutions. In the melt synthesis, the mixture of oxides or their precursors is rapidly (1–60 s) melted by irradiation with intense light in an arc-imaging furnace. A spherical molten sample in which cations were mixed homogeneously was directly solidified on a copper hearth with rapid cooling of 10^2 K/s. $LaAlO_3$, $GdScO_3$, $ATiO_3$ (A = Ba, Sr and Ca), and their mixed solid solutions were synthesized by use of this technique [28].

Tian et al. reported preparation of pure $LaAlO_3$ powder by combustion synthesis from a concentrated solution of the nitrates of lanthanum and aluminate as oxidizer and glycine acid as fuel, with the objective of obtaining nano-sized crystallites of the material with high specific area at relatively low temperature. Precursor powders and calcined powders were characterized by DTA, TGA, XRD, and TEM. The results showed that pure perovskite $LaAlO_3$ powder of particle size 78–100 nm was formed by treatment at 700 °C for 2 h. The specimen sintered at 1,500 °C for 12 h had maximum bulk density and the best microwave dielectric properties: $\varepsilon_r = 23$ and $Q_f = 38{,}000$ GHz [29].

Kuo et al. reported preparation of nano-crystalline lanthanum monoaluminate ($LaAlO_3$) powders by chemical coprecipitation and use of 25 % *v*/*v* NH_4OH, 0.05 M $La(NO_3)_3{\cdot}6H_2O$, and 0.05 M $Al(NO_3)_3{\cdot}9H_2O$ aqueous solutions as starting materials. Fourier-transform IR spectroscopy (FTIR), TGA–DTA, XRD, Raman spectrometry, specific surface area (BET) analysis, SEM, TEM, and electron diffraction (ED) were used to characterize the $LaAlO_3$ powders obtained. The crystallization temperature of the $LaAlO_3$ precursor gels precipitated at pH 9 was estimated to be 810 °C by TGA–DTA. The XRD patterns of $LaAlO_3$ precursor gels precipitated at pH 8–12 and calcined at 700 °C for 6 h contained a broad arciform continuum between 24° and 32° and sharp peaks of $LaAlO_3$, except for precursor gels precipitated at pH 9. When the $LaAlO_3$ precursor gels were precipitated at pH 9 and calcined at 700 °C for 6 h the perovskite $LaAlO_3$ phase was formed, and the presence of crystalline impurities was not observed. The crystallite size of $LaAlO_3$ increased slightly from 37.8 to 41.5 nm when the calcination temperature was increased from 700 to 900 °C for 6 h. $LaAlO_3$ powders prepared by chemical co-precipitation have a very large specific surface area of 30 m^2 g^{-1}. The relative density is >97 % when these nano-crystalline $LaAlO_3$ powders are sintered at 1,550 °C for 2 h [30].

Li et al. reported synthesis of rhombohedral $LaAlO_3$ powder by reacting equimolar La_2O_3 and Al_2O_3 in a molten KF–KCl eutectic salt for 3 h between 630 and 800 °C. The lowest synthesis temperature (630 °C) is approximately 1,000 degrees below that of conventional mixed oxide synthesis, and close to or lower than those used by most wet chemical methods. $LaAlO_3$ particle size increased from <3 to 3–7 μm when the temperature was increased from 630 to 700 °C, but changed little on further increasing the temperature to 800 °C. Particle size decreased when the salt-to-oxide weight ratio was increased from 1:1 to 6:1. The "dissolution–precipitation" mechanism is important in the molten salt synthesis of $LaAlO_3$ [31].

Behera et al. reported that $LaAlO_3$ ceramic powders could be prepared from metal chlorides by a combined gel precipitation process using ammonia. The conventional gel precipitation technique was slightly modified by introducing an ultrasonication step followed by centrifugal washing of the gel. The dried gels produced pure-phase $LaAlO_3$ powders on calcination of the combined gel-precipitated (GP) powders at 1,100 °C and calcination of the washed gel (WG) at 600 °C. The phase evolution was studied and it was found that the delay in obtaining monophasic $LaAlO_3$ in the combined GP powder was because of crystallization of an impure phase, LaOCl. This phase was not detected in the WG powders. TEM micrographs revealed uniform morphology of the calcined WG powders, in contrast with the irregular particles in the GP powders. The uniform morphology was attributed to ultrasonic effects during washing of the gel [32].

Ran et al. reported successful synthesis of $LaAlO_3$ powders by pyrolysis of complexes of lanthanum and aluminum with TEA. The precursors and the derived powders were characterized by simultaneous TGA and DSC analysis, XRD, specific surface area measurements, and TEM. Pure $LaAlO_3$ phase was obtained at 775 °C for 2 h or 750 °C for 4 h, without formation of any intermediate phase. TEM images revealed pores in $LaAlO_3$ powders prepared at 800 °C for 2 h [12].

Luo et al. reported investigation of the stable structure, phase transition, and elastic properties of $LaAlO_3$ by use of first principles linearized augmented plane wave calculations within density functional theory. Calculation reveals that at low temperatures the rhombohedral *R*-3*C* phase is the most energetically stable of the three proposed structures: *R*-3*C* (No. 167), *R*-3*M* (No. 166), and *R*-3*C* (No. 161). It was found that $LaAlO_3$ is transformed from the rhombohedral *R*-3*C* phase to the cubic *PM*-3*M* phase, with a volume change of 1 %, when the applied hydrostatic pressure is 15.4 GPa; this is consistent with experimental results. The elastic constants, shear modulus, bulk modulus, and Poisson's ratio of $LaAlO_3$ were calculated and compared with corresponding experimental data. The results showed that rotation of the AlO_6 octahedra in $LaAlO_3$ substantially affects the anisotropic elastic constants. From the calculated Debye temperature and elastic constants, the *R*-3*C* phase of $LaAlO_3$ is predicted to be more thermostable and have greater fracture toughness than the high-pressure-generated *PM*-3*M* phase [33].

Deren et al. investigated $LaAlO_3$ single crystals doped with Tm^{3+} ions. After continuous-wave excitation of the $^3F_2$ level (at approx. 15,115 cm^{-1}) strong violet and UV light were observed, corresponding to the $^1D_2 \rightarrow {}^3F_4$ (22,000 cm^{-1}), $^1D_2 \rightarrow {}^3H_6$ (27,700 cm^{-1}), and $^3P_0 \rightarrow {}^3F_4$ (28,600 cm^{-1}) transitions. Emission and excitation spectra of the Stokes and anti-Stokes emission were measured. The excitation and absorption spectra were compared and the power dependence of the anti-Stokes emission was recorded and analyzed. Possible mechanisms of ESA and cross-relaxation involving three or more photons are discussed [34].

Luo et al. investigated the electronic structure, chemical bonding, and optical properties of rhombohedral $LaAlO_3$ by use of the full potential linearized augmented plane wave (FP-LAPW) method with the generalized gradient approximation (GGA). Analysis of the electronic density profile, Mulliken charge, and bond population revealed both covalent and ionic nature of the chemical bonding. The calculated complex dielectric function is consistent with experimental results from UV spectroscopic ellipsometry measurement. The optical spectra were assigned to the interband transition from O valence to La conduction bands in the low-energy region. The absorption spectrum, the electron energy-loss spectrum, optical conductivity, reflectivity, and refractive index were, furthermore, derived from the complex dielectric function. The absorption spectrum is indicative of an optical band gap of 6.1 eV, which is consistent with several other experimental measurements [35].

Singh et al. prepared holmium-doped $LaAlO_3$ powder phosphors at furnace temperatures as low as 500 °C by combustion without further calcination. Powder XRD and FTIR spectrometry measurements were used to characterize the products, and their optical properties were studied by use of UV–visible–NIR and PLS. The J–O model was used to obtain oscillator strengths (*f*) and three phenomenological intensity values. By use of J–O values (Ω_2, Ω_4 and Ω_6) the radiative transition probabilities (A_{ab}), radiative lifetimes (τ_R), and branching ratios were calculated for some excited states of Ho^{3+}. By use of the Fuchtbauer–Ladenberg formula, the stimulated emission cross-sections (semi) for some interesting transitions, for example $^5S_2 \rightarrow {}^5I_8$ and $^5F_5 \rightarrow {}^5I_8$, of Ho^{3+} in $LaAlO_3$, were determined and discussed [36].

Deren et al. reported the spectral and laser properties of an Nd^{3+}-doped (1 % *w*/*w*) $LaAlO_3$ single crystal. The energy levels of the Nd^{3+} ion in the $LaAlO_3$ matrix were assigned. The J–O values $\Omega_2 = 1.346$, $\Omega_4 = 4.490$, and $\Omega_6 = 5.168$ (all $\times 10^{-20}$ cm^{-2}) were evaluated. The absorption σ_{abs} and emission σ_{emi} cross-sections at the respective pumping and emission wavelengths were calculated to be $\sigma_{abs}(789.7\ nm) = 2.42 \times 10^{-20}\ cm^2$, $\sigma_{emi}(909\ nm) = 5.02 \times 10^{-20}\ cm^2$, and $\sigma_{emi}(1{,}080\ nm) = 7.03 \times 10^{-20}\ cm^2$. Continuous-wave laser action at 1,080 nm was obtained for $LaAlO_3:Nd^{3+}$ [37].

Gocalinska et al. reported results from spectroscopic research on an $LaAlO_3$ crystal doped with Tm^{3+} ions. The host has the perovskite structure. The investigated sample was a single crystal grown by the Czochralski method. Absorption, emission, and decay profiles were measured in the visible and IR regions at room and low (77 K) temperature. By excitation matching emission from several excited states of the $^1D_2$ (27,700 cm^{-1}), $^1I_6 + {}^3P_0$ (28,600 cm^{-1}), $^3H_4$ (12,400 and 6,800 cm^{-1}), and $^3F_4$ (5,800 cm^{-1}) levels was obtained; with these strong bands other weaker transitions were also recorded. The decay times were short for the violet and blue emission and significantly longer for the red and IR emission (at room temperatures the values were 22 ls and 5.8 ms for the $^1D_2$ and $^3F_4$ levels, respectively). The system is discussed in terms of Tm^{3+} energy level structure. Further investigations are being considered [38].

Kharlamova et al. reported preparation of Al and Sr-doped apatite-type lanthanum silicates (ATLS) by mechanochemical activation (MA) and use of the Pe method; some structural and electrical properties of the doped samples were studied. MA results in ATLS formation even at room temperature after 20–35 min activation. Synthesis by the Pe method occurs via a solid-state reaction mechanism. MA of carbonate precursors obtained by use of the Pe method results in the formation of a single-phase ATLS after annealing at 900 °C. For Al-doped apatite samples, formation of $LaAlO_3$ as a secondary phase is observed at high substitution levels, depending on sample stoichiometry, which affects the properties of ceramics obtained [39].

Deren et al. reported calculation of rates of multiphonon non-radiative transitions, W_{MNR}, from rates of radiative transitions and measured emission decay times for praseodymium, neodymium, erbium, holmium, and thulium ion-doped $LaAlO_3$.

Radiative transition rates were determined on the basis of J–O theory. The results obtained were plotted as a function of energy gap DE and fitted by use of an exponential function $W_{\mathrm{MNR}} = B \cdot \exp(-\alpha \cdot \Delta E)$, where $B = 1.02 \times 10^9$ and $\alpha = 3.61 \times 10^{-3}$. Fitting results showed that rates of multiphonon non-radiative transition were low compared with those of other oxide crystals, and were similar to those of YAG [40].

Chang et al. reported that $LaAlO_3$ had potential as a gate dielectric for future very-large-scale integration devices. In this work, metal-oxide–semiconductor capacitors and transistors were fabricated with $LaAlO_3$ gate dielectric and the electron mobility degradation mechanisms were studied. The $LaAlO_3$ films were deposited by radiofrequency magnetron sputtering. The $LaAlO_3$ films were examined by XRD, secondary ion mass spectroscopy, and X-ray PLS. The temperature dependence of metal-oxide–semiconductor field-effect transistor characteristics was studied from 11 to 400 K. The rate of threshold voltage change with temperature ($\Delta V_T/\Delta T$) was -1.51 mV/K. Electron mobility, which is limited by surface roughness, is proportional to $E_{\mathrm{eff}}^{-0.66}$ in electric fields of $0.93 < E_{\mathrm{eff}} < 2.64$ MV/cm at 300 K and phonon scattering is proportional to $T^{-5.6}$ between 300 and 400 K. Soft optical phonon scattering was used to explain the extra source of phonon scattering in $LaAlO_3$-gated *n*-channel metal-oxide–semiconductor field-effect transistors [41].

Liu et al. reported preparation of nano-crystalline $LaAlO_3{:}Sm^{3+}$ phosphors by a Pe-type sol–gel process. XRD, field emission SEM (FESEM), PL, and cathodoluminescence (CL) spectra were used to characterize the synthesized phosphors. XRD results revealed that the sample begins to crystallize at 600 °C, and the pure $LaAlO_3$ phase can be obtained at 700 °C. FESEM images indicate that the Sm^{3+}-doped $LaAlO_3$ phosphors are composed of aggregated spherical particles with sizes ranging from 40 to 80 nm. On excitation of the Sm^{3+}-doped $LaAlO_3$ phosphors by UV light (245 nm) or low-voltage electron beams (1–3 kV) the characteristic yellow emission of Sm^{3+} ($^4G_{5/2}$–$^6H_{5/2}$, $^6H_{7/2}$, $^6H_{9/2}$ transitions) is observed. The CL intensity (brightness) of the Sm^{3+}-doped $LaAlO_3$ phosphor is greater than that of the commercial product [Zn (Cd) $S{:}Ag^+$] (yellow) [42].

Chandradass et al. reported synthesis of pure $LaAlO_3$ nano-powders by use of an emulsion precursor derived from a mixed-metal and oleic acid solution. The precursors and derived oxide powders were characterized by DTA, TGA, IR spectroscopy, XRD, and TEM. The pure $LaAlO_3$ phase was synthesized at 800 °C for 2 h, in air, directly from amorphous precursors, without formation of an intermediate phase. The average particle size determined by TEM was 60 nm. FTIR analysis was used to monitor elimination of the oleic acid from the emulsion-derived precursor and calcined powder [43].

Yu et al. reported synthesis of pure $LaAlO_3$ nanoparticles by use of a citrate-precursor technique. $La(NO_3)_3$, $Al(NO_3)_3$, and $C_3H_4(OH)(COOH)_3$, in the molar ratio 1:1:4.5, were dissolved in deionized water. The pH of the aqueous solution was adjusted by use of aqueous NH_3. After drying, the citrate precursors were charred at 350 °C, then calcined at different temperatures. The thermochemical behavior of the charred citrate precursor in the formation of $LaAlO_3$ was investigated by use of XRD, IR spectroscopy, TGA, and DTA. Whereas the charred specimen obtained at pH 2 (without addition of aqueous NH_3) was composed of $LaAl(OOCH_2)_3$ the charred specimens obtained at $pH > 2$ were composed of $LaAlO_{3-x-y}(CO_3)_x$

$(OH)_{2y}$. All these metallic salts were decomposed at temperatures between 600 and 780 °C to form crystalline $LaAlO_3$ but calcination of the specimens in air at $\geq$800 °C was required to remove all residual charring and produce pure $LaAlO_3$. At 900 °C, the citrate-derived particles obtained at $pH > 2$ were composed of $LaAlO_3$ crystallites of average size ~30 nm [44].

Tian et al. reported preparation of spherical $LaAlO_3$ nanoparticles in a reverse microemulsion consisting of solution (water phase), Tween-80 and Span-80 (surfactant), *n*-butanol (cosurfactant), and cyclohexane (oil phase). Precursor powders and calcined powders were characterized by DTA, TGA, XRD, and TEM. Pure perovskite $LaAlO_3$ was formed when the precursor hydroxides were calcined at 800 °C for 2 h. Particle size was approximately 50 nm and the monodisperse particles were spherical. By use of the reverse microemulsion process the crystallization temperature of $LaAlO_3$ can be dramatically reduced by approximately 700 °C compared with that used in the classical solid-state reaction method [45].

Chandradass et al. reported synthesis of lanthanum monoaluminate ($LaAlO_3$) nanoparticles by use of microreactors containing poly(oxyethylene) nonylphenyl ether (Igepal CO-520)–water microemulsions. Control of particle size was achieved by varying the water-to-surfactant molar ratio. The synthesized and calcined powders were characterized by TGA–DTA, XRD analysis, SEM, TEM, and FTIR spectroscopy. DTA showed that $LaAlO_3$ phase transformation decreased with increasing water-to-surfactant ratio. The pure $LaAlO_3$ phase was synthesized, without formation of intermediate phase, by direct annealing of the amorphous precursors at 800 °C for 2 h in air. The average particle size was found to increase with increasing water-to-surfactant ratio. FTIR analysis was used to monitor elimination of residual oil and surfactant phases from the microemulsion-derived precursor and calcined powder [46].

Negahdari et al. reported synthesis of nano-crystalline $LaAlO_3$ powder by calcination of a precursor prepared by evaporation of an aqueous solution of sucrose, PVA, and stoichiometric amounts of the desired Al and La nitrates. Phase evaluation (XRD) in conjunction with thermal analysis (DTA–TGA) showed that pure nano-crystalline $LaAlO_3$ phase powder was obtained at temperatures between 600 and 700 °C. The average crystallite size of the synthesized powder, obtained by Rietveld analysis and TEM, was approximately 30 nm. Average particle size, as determined by FESEM, was <100 nm. The average specific surface area of the powder was very high ~43 $m^2\ g^{-1}$. According to the electrokinetic behavior of synthesized $LaAlO_3$ power, it had a point of zero charge (pzc) at approximately pH 9.9 [47].

Boudali et al. studied the structural, elastic, and electronic properties of perovskite $LaAlO_3$ by use of two different methods—the FP-LAPW method and the pseudopotential plane wave scheme with the GGA. They evaluated ground-state quantities, for example lattice properties, bulk modulus, and pressure derivative, and the elastic constants. They also reported results from measurement of band structure, densities of states, and charge densities. These results were in good agreement with previous theoretical work and other experimental results. To complete determination of the fundamental characteristics of this compound they analyzed the thermodynamic properties by use of the quasi-harmonic Debye model [48].

Deren et al. studied the symmetry of $LaAlO_3$ nano-crystals as a function of crystallite size. Properties of $LaAlO_3$ nano-crystallites obtained by the precipitation method; doped praseodymium and chromium ions were examined spectroscopically. By use of Raman spectroscopy, HRTEM, XRD, and electronic spectroscopy they proved that the symmetry of $LaAlO_3$ crystallites depends on their size. At room temperature the smallest crystals obtained (average size $\sim$5 nm) have cubic symmetry whereas the largest (average size >110 nm) have rhombohedral symmetry. Possible explanations for this phenomenon were discussed [10].

Zhang et al. reported construction of the complete d^3 energy matrix, including the cubic crystal field, coulombic interactions, spin–orbit coupling, and the low-symmetry crystal field, for $LaAlO_3:Cr^{3+}$ on the basis of the strong scheme of ligand field theory and non-coupling trigonal bases. By diagonalizing the complete d^3 energy matrix, the energy levels, wavefunctions, and crystal-field data were calculated for $LaAlO_3:Cr^{3+}$ at normal pressure. The g factor of the ground state under normal pressure and low temperature was calculated on the basis of these results and proved to be consistent with experiment data. By taking into account the wavefunctions and thermal shift theory, the thermal shifts of the R_1 line of $LaAlO_3:Cr^{3+}$ were calculated and the related values were determined. All the results were in good agreement with experimental results. The results also revealed more completely the physical origin and micro-mechanism of R_1 line thermal shifts [49].

Mao et al. used the PL and lifetime decay properties of Eu of different valence to investigate the mechanism of emission of green luminescence at $\sim$515 nm for full color emission $LaAlO_3$ phosphors co-doped with Eu^{2+} and Eu^{3+}. The green emission was assigned to enhanced $^5D_2 \rightarrow {}^7F_3$ transition emission of Eu^{3+}. Energy transfer between Eu^{2+} and the $^5D_2$ level of Eu^{3+}, resulting in enhancement of the $^5D_2 \rightarrow {}^7F_3$ transition emission, was proposed. In addition, energy-transfer relationships between host Eu and charge transfer state-Eu were also discussed, in relation to PLE (PL of excitation) spectra and band schemes [50].

Liu et al. motivated by the recent discovery of superconductivity at the $LaAlO_3$–$SrTiO_3$ heterointerface, conducted a theoretical investigation of impurity-induced resonance states with coexisting spin singlet s-wave and triplet p-wave pairing symmetries by considering the effect of Rashba-type spin–orbit interaction (RSOI). Because of the nodal structure of the mixed gap function, single non-magnetic impurity-induced resonance peaks occur in the local density of state. They also analyzed, by point contact tunneling and scanning tunneling microscopy, the evolution of density of states and local density of states with the weight of the triplet pairing component determined by the strength of the RSOI, which will be widely observed in thin films of superconductors with surface or interface-induced RSOI or different non-centrosymmetric superconductors, and thus shed light on the admixture of the spin singlet and RSOI-induced triplet superconducting states [51].

Deren et al. reported the preparation, by the precipitation method, and spectroscopic properties of nano-sized crystallites of $LaAlO_3$ doped with Pr^{3+} (1 mol%) and traces of Cr^{3+} ions. A new material was obtained with spectroscopic properties differing nominally from those of the same bulk of $LaAlO_3:Pr^{3+}$. It was observed that when the diameter of the nano-$LaAlO_3$ sample was >110 nm the perovskite structure changed from cubic to rhombohedral. As a result, the intensity of emission by larger samples was two orders of magnitude higher than that for smaller samples [52].

Malinowski et al. investigated the concentration-dependent emission spectra and fluorescence dynamic profiles of $Pr_xLa_{1-x}AlO_3$ single crystals to better understand the processes responsible for concentration quenching of the praseodymium $^3P_0$ and $^1D_2$ emissions. The rates of cross-relaxation transfer were experimentally determined as a function of Pr^{3+} concentration. Decays were modeled and nearest-neighbor trapping rates were calculated [53].

Mortada et al. studied initial Si growth mechanisms on $LaAlO_3$ (001), a crystalline oxide with a high dielectric constant (high-*k* material). The clean $LaAlO_3$ (001) substrate has a c(2 × 2) structure that can be attributed to surface O vacancies. Deposition of Si by molecular beam epitaxy was studied as a function of both deposition temperature and thickness. Epitaxy was obtained only above 550 °C. In this case, a Volmer–Weber mode is observed. The associated nano-dots are relaxed and formed by pure Si, as ascertained by monitoring the Si_{2s} XPS peak, which remains for 1 and 10 ML at the binding energy corresponding to Si–Si bonds. Moreover the islands have an abrupt interface with the $LaAlO_3$ (001) substrate without formation of silicate or silica. A unique epitaxial relationship between $LaAlO_3$ and the crystallized Si islands, in which the Si (001) planes are parallel to the $LaAlO_3$ (001) planes, but rotated by 451 in the (001) direction, is indicated by RHEED (reflection high-energy ED) and confirmed by HRTEM. This orientation leads to mismatch and strain minimization of the Si film [54].

Dudek et al. reported the luminescence properties of Y_2O_3 and $LaAlO_3$ nano-powders doped with Pr^{3+} ions and of PMMA (poly(methyl methacrylate))-based composite materials doped with these powders. Active nano-powders differing in praseodymium ion concentration were prepared by use of a sol–gel method and their emission properties in the visible spectral range were carefully characterized. In particular, the excitation and emission spectra were measured, with their fluorescence decay profiles, and the differences between the optical properties of these materials were discussed and compared with data available for the bulk materials. Finally, PMMA-based composite materials doped with $Pr^{3+}:Y_2O_3$ and $Pr^{3+}:LaAlO_3$ nano-powders were manufactured and characterized. The results obtained showed that polymer composites doped with active nano-powders tended to retain the luminescence properties of the original nano-powders [55].

Yu et al. reported the synthesis of crystalline $LaAlO_3$ nanoparticles at relatively low temperatures by use of a citrate-precursor technique. $La(NO_3)_3$, $Al(NO_3)_3$, and $C_3H_4(OH)(COOH)_3$, in the molar ratio 1:1:1, were dissolved in deionized water. Aqueous NH_3 was used to adjust the aqueous solution to pH 7. After drying, the citrate precursors were charred at 350 °C, followed by calcination at different temperatures, in air or oxygen atmosphere. The thermochemical properties of the resulting particles were analyzed by use of TGA and DTA, XRD, IR spectroscopy, SEM, and TEM. Effects of calcination temperature and heating atmosphere on the formation of crystalline $LaAlO_3$ nanoparticles were investigated. In O_2 atmosphere, calcination of the citrate-derived charred solid precursor at 700 °C for 3 h decomposed all intermediates, producing pure $LaAlO_3$ nanoparticles (particle size $\leq$100 nm) with an average crystallite size of approximately 24 nm and high sinterability [56].

Liu et al. studied the pulsed laser deposition and growth of a high-*k* dielectric lanthanum aluminate $LaAlO_3$ (LAO) thin film on an indium tin oxide–glass substrate at different oxygen partial pressure. On the basis of a pulsed laser deposition growth mechanism we can explain how different oxygen partial pressures affect surface roughness, formation of an interfacial layer, and the transparent resistive switching characteristics of LAO thin films. The micro-structure and oxygen concentration difference inside LAO thin films may be the main reason for the different electrical and resistive switching properties. Films grown at higher oxygen partial pressure had more reliable resistive switching performance, because of formation of the interfacial layer and a lower concentration of oxygen vacancies. The interfacial layer serves as a good oxygen reservoir and the involvement of more oxygen ions ensures switching reliability. Migration of oxygen ions between the interfacial layer and the LAO film under the applied bias may be the switching mechanism [57].

Yamasaka et al. reported that, by measuring electron spin resonance (ESR) spectra at the X-band frequency and absorption spectra from the visible to UV region at room temperature, they confirmed that perovskite single-crystal $LaAlO_3$ contains Cr and Fe as impurities. When $LaAlO_3$ is exposed to photons with energy >4.5 eV, the intensities of ESR signals from Cr^{3+} and Fe^{3+} decrease, which indicates that electrons released by the photon irradiation are captured by Cr^{3+} and Fe^{3+}. Concurrently with this, a broad optical absorption band at approximately 3.0 eV and two new broad and weak ESR signals appear. The former was attributable to a combination of a hole and an La^{3+} (or Al^{3+}) vacancy, and the two weak ESR signals were assigned to the O^- center and F^+ center [58].

Maczka et al. reported the synthesis of $LaAlO_3$, $La_{0.9}Dy_{0.1}AlO_3$, $La_{0.9}Er_{0.1}AlO_3$, and $La_{0.8}Dy_{0.1}Er_{0.1}AlO_3$ nano-crystalline powders by a two-step process combining a mechanically induced metathesis reaction and molten salt synthesis. The proposed two-step method gives ready access to pure and/or doped perovskite-type $LaAlO_3$ nano-powders at remarkably low temperatures, i.e., even at 350 °C although firing at 500 °C is needed to obtain the pure phases. The samples obtained were characterized by XRD, TEM, Raman, IR, and luminescence methods. These methods showed that mean crystallite size is approximately 50–60 nm and the $LaAlO_3$ nano-crystallites have the $R\bar{3}c$ structure, the same as for bulk $LaAlO_3$. The Raman spectrum of nano-crystalline $LaAlO_3$ is very similar to that of bulk. In contrast with this behavior, IR spectra of the synthesized compounds were significantly different from the IR spectrum of bulk $LaAlO_3$. The origin of this behavior was discussed. Luminescence study showed that cross-relaxation processes quench the emission of samples doped with Dy^{3+} and Er^{3+} [59].

Khamkar et al. reported obtaining nano-structured $LaAlO_3$ by self-combustion synthesis using lanthanum nitrate and aluminium nitrate as precursors and glycine as fuel, without subsequent heat treatment after synthesis. The effect of temperature variation was investigated for a sample of constant molar ratio. The crystallinity (phases present and crystallite size: estimated by the single-line method) of the product obtained was determined by XRD measurement, TGA–DTA, SEM, and TEM. This synthetic method facilitated production of perovskite $LaAlO_3$ with crystallite size between 40 and 70 nm [60].

Djoudi et al. reported the synthesis and characterization of lanthanum monoaluminate $LaAlO_3$ by the method of co-precipitation. The powder was successfully synthesized by use of NaOH, $La(NO_3)_3 \cdot 6H_2O$, and $Al(NO_3)_3 \cdot 9H_2O$ as raw materials and calcination at different temperatures. It was characterized by several techniques: FTIR, TGA–DTA, XRD, and laser diffusion. All the results from physicochemical characterization showed that the crystallization temperature of the precipitated $LaAlO_3$ precursor gels was 790 °C. The XRD pattern showed that calcination of the $LaAlO_3$ precursor gels at 700 °C for 6 h results in a rhombohedral hexagonal phase with the perovskite structure; the presence of crystalline impurities was not detected. The crystallite size of $LaAlO_3$ increased slightly from 31 to 44.5 nm when the calcination temperature was increased from 700 to 1,000 °C, again for 6 h [61].

Mendoza et al. reported the preparation of perovskite-type $LaAlO_3$ nanoparticles by a facile, rapid, and environmentally benign molten-salts method in which alkali metal nitrates were used as low-temperature fluxes. Starting from hydrated lanthanum and aluminum nitrates and alkali metal hydroxides, the proposed method consists of two steps—a mechanically induced metathesis reaction then brief firing at temperatures above the melting points of the nitrates. The purpose of the first step is twofold—in situ generation of the alkali metal nitrate flux and formation of an La and Al-containing precursor material suitable for synthesis of bulk $LaAlO_3$ nanoparticles in molten nitrates. Different alkali metal nitrates and eutectic mixtures were used to investigate the effect of melt basicity in the reaction outcome. Single-phase $LaAlO_3$ was obtained directly, without any purification step, by use of three molten media: $LiNO_3$, $NaNO_3$, and their mixture; use of KNO_3 as flux, either alone or as part of eutectic compositions, prevents complete conversion, and the material is obtained mixed with additional crystalline phases, for example lanthanum hydroxynitrates and carbonates. As-prepared $LaAlO_3$ powders are composed of loosely agglomerated nanoparticles with very fine crystallite size (32–45 nm). This method results in substantially reduced synthesis times and temperatures compared with other methods used to prepare this material [62].

Li et al. reported that the gap states of the oxygen vacancy in $LaAlO_3$ and related high-dielectric constant (high-*k*) perovskite oxides can be passivated by fluorine, or by substitution with nitrogen or alkaline earth metal atoms at adjacent sites. The mechanism is completion of the electron shell by the substitutions, and repulsion of the now empty vacancy gap state into the conduction band by relaxation of the adjacent Al and La ions away from the vacancy because it is locally $+2$ charged [63].

Murtaza et al. reported, for the first time, investigation of the structural and optoelectronic properties of $LaAlO_3$ under pressure by use of the highly accurate all electrons FP-LAPW method. The calculated lattice parameter at zero pressure was in excellent agreement with the experimental results. Furthermore, with increasing external pressure the lattice constant and bond lengths decrease in accordance with the experimental results. The compound at zero pressure is an indirect band gap semiconductor; interestingly the indirect nature shifts to direct with increasing pressure. The bonding in the material is of mixed covalent and ionic nature. The frequency-dependent optical properties, for example the real and imaginary parts of the dielectric function, refractive index, reflectivity, optical conductivity, absorption coefficient, and sum rules were calculated under pressure [64].

Jang et al. reported successful growth of epitaxial $LaNiO_3$ (1u.c.)–$LaAlO_3$ (1u.c.) superlattices on single-crystal $LaAlO_3$ (001) substrates by use of the pulsed laser deposition method. Specular RHEED intensity oscillations were repeated continuously throughout the entire growth. Large angle θ–2θ X-ray scans showed only peaks from the superlattices and substrates. These results confirm the highly qualified crystal structure of the superlattices. The temperature dependence of the resistivity has semiconducting behavior in the entire temperature range studied. These observations indicated that the semiconducting characteristics of the superlattice can be attributed to radical alteration of the electronic structure of the NiO_2 layers [65].

Maczka et al. synthesized $LaAlO_3$ nanoparticles doped with Eu^{3+} and Er^{3+} ions, at 500 °C, by a two-step process which combined a mechanically induced metathesis reaction with molten salt synthesis. The samples obtained were characterized by XRD and TEM, which showed the mean crystallite size was ~45 and ~57 nm, respectively. Furthermore, excitation and luminescence spectra and decay profiles were measured for the synthesized samples. These studies suggested that the Eu^{3+} ions are located at three different sites without inversion symmetry, and also revealed up-conversion emission in the samples doped with Er^{3+} ions. The up-conversion mechanism was discussed [66].

Li et al. reported preparation of $LaAlO_3$ powders by use of a simple polymer-complexing plus combustion method with PVA or PEG (poly(ethylene glycol)) as complexing agent and fuel. The effect of different polymers on phase purity, powder morphology, and sintering performance was investigated. Trace amounts of the impurity La_2O_3 were present in the PEG powder, but could be eliminated after high temperature sintering. The pure $LaAlO_3$ phase was readily obtained by calcination of PVA powders at 950 °C, although severe aggregation was always observed. PEG has advantages over PVA in terms of densification and microstructure control during the sintering process. High relative density of 97.0 % and homogeneous fine microstructure with grain size <3 μm can be obtained for PEG-derived samples sintered at 1,600 °C for 5 h. To obtain better quality $LaAlO_3$ powders by combustion, PEG is preferred to PVA [67].

Dhahri et al. reported synthesis of Eu^{3+}-doped $LaAlO_3$ nano-phosphors by a combustion process. They used a concentrated solution of lanthanum nitrates and aluminate as oxidizer, and glycine acid as fuel. The powders were characterized by IR spectroscopy, XRD, SEM, TEM, and fluorescence spectroscopy. The pure $LaAlO_3$ phase was obtained by heating at 800 °C for 4 h, without formation of any intermediate phase, with an average crystal size, as determined by TEM, of 60 nm. Intense PL emission was reported at 616 nm, enabling use of this material as a red phosphor [68].

Watras et al. measured the optical properties of two series of perovskites (first: $LaAlO_3$, $GdAlO_3$ and $YAlO_3$ and second: $LaAlO_3$, $LaGaO_3$ and $LaScO_3$) doped with 1 % Ce^{3+} ions. The results obtained enabled estimation of values of the centroid shift (ε_c) and crystal-field splitting (ε_{cfs}). The effects on ε_c and ε_{cfs} of ionic radii, electronegativity of cations, and distortion of structure were determined [69].

Comparative study of the literature

A comparative study of the literature is given in Table 1.

Table 1 Comparative study of the review literature

Synthesis	Characterization	Study	Remarks	Ref.
Evaporation method	XRD, IR, TGA, DTA	Dielectric properties	Simpler, cost effective, more time and energy efficient method of preparing ultrafine, homogeneous, single-phase $LaAlO_3$	[4]
Two separate methods of chemical powder preparation: homogeneous precipitation and self-propagating combustion synthesis	XRD, TGA, DTA, SEM, ED X-ray spectroscopy	–	Lowest ever synthesis temperature (650 °C)	[15]
–	–	$LaAlO_3$ (100) surface	LaO surface has lowest surface energy, it is the most probable surface termination	[16]
Polymerized complex route	XRD, TG–DTA,	–	No impurities, fine powders with large surface areas	[17]
Citrate precursor	–	Structural properties and adsorptive behavior of catalyst towards oxygen	–	[18]
Laser molecular beam epitaxy (LMBE)	AFM, XRD, HRTEM	Crystallinity, surface	Good crystallinity, surface smoothness, suitable for use in new generation of microelectronic devices	[21]
Pechini's method	XRD, TEM	Luminescence decay	Luminescence lifetimes enhanced with decreasing nano-crystal sizes	[26]
Czochralski method by Union Carbide, USA	–	Anti-Stokes emission	ESA is a strong up-conversion phenomenon, both Stokes and anti-Stokes emission are observed, green emission dominates the visible up-converted emission, power dependance of anti-Stokes emission depends on excitation wavelength	[27]
Melt synthesis technique	XRD	–	Method is suitable for material research in high temperature synthesis	[28]
Combustion synthesis	DTA, TGA, XRD, TEM	Dielectric properties, particle size	Best microwave dielectric properties, maximum bulk density, particle size range 78–100 nm	[29]

Table 1 continued

Synthesis	Characterization	Study	Remarks	Ref.
Chemical co precipitation	FTIR, TGA–DTA, XRD, BET, SEM, TEM, ED	Thermal behavior, crystal structure, crystallite size, sintering behavior	Lowest process temperature (700 °C), perovskite $LaAlO_3$ phase with no crystalline impurities, crystallite size increases from 37.8 to 41.5 nm with increase in calcination temperature from 700 to 900 °C, large specific surface of 17–29 $m^2 g^{-1}$, relative density is 98.7 % when sintered at 1,550 °C for 2 h	[20]
Molten salt synthesis	XRD, XRF, SEM, EDS	Effect of temperature on particle size	Lowest synthesis temperature (630 °C), particle size increases from 630–700 °C then decreases with further increase in temperature (800 °C)	[31]
Combined gel precipitation process	TEM, PA-FTIR, DTA, TGA, XRD	Phase evolution, morphology	Fairly spherical morphology of $LaAlO_3$ powders with size ~25 nm and narrow size distribution (wet gel method), polydispersed and irregular morphology for powders (gel precipitation method), control of particle dispersion in suspension effectively improves the powder characteristics and reduces the phase-formation temperature	[32]
Pyrolysis (thermal decomposition)	TG, DSC, XRD, TEM, specific surface area measurement	–	Porous $LaAlO_3$ powder	[12]
–	–	Stable structure of $LaAlO_3$, phase transition, elastic properties	*R*-3*C* phase of $LaAlO_3$ is more thermostable and has greater fracture toughness than high-pressure *PM*-3*M* phase	[33]
Czochralski method by Union Carbide, USA	–	Up-conversion processes, optical properties	$LaAlO_3$:Tm^{3+} has strong ability to give anti-Stokes emission, high efficiency of ESA	[34]
–	–	Electronic structure, chemical bonding and optical properties	Combination of covalent and ionic nature in chemical bonding of rhombohedral $LaAlO_3$, optical band gap of 6.1 eV	[35]

Table 1 continued

Synthesis	Characterization	Study	Remarks	Ref.
Combustion route	XRD, FTIR	Optical properties	Safe, rapid, simple and reliable technique for synthesis of fine powder of $LaAlO_3:Ho^{3+}$, two transitions have high emission cross-section and thus are more efficient for laser action	[36]
Czochralski method by Union Carbide, USA	–	Spectral and laser properties of $LaAlO_3:Nd^{3+}$	Long decay time, continuous-wave laser action at 1,080 nm, low value of emission cross-section at the laser emission (7.03×10^{-20} cm^2) makes the crystal favorable for passively Q-switched laser action	[37]
Czochralski method by Union Carbide, USA	–	Multiphonon transitions	W_{MNR} (multiphonon non-radiative transition rate) of a particular transition of an ion differs very much from the obtained fitting which indicates that additional non-radiative mechanisms are involved	[40]
Radiofrequency magnetron sputtering (depositing $LaAlO_3$ film)	XRD, XPS, SIMS	Electron mobility degradation mechanism	Temperature dependance of electron mobility on the vertical field reveals the difference between $LaAlO_3$ and SiO_2-gated transistors, coulomb scattering is approximately the same for both, surface scattering and phonon scattering of $LaAlO_3$-gated MOSFETs are more severe than those of SiO_2-gated n-MOSFETs, transverse soft optical phonons are used to explain the extra source of phonon scattering in $LaAlO_3$-gated n-MOSFETs	[41]
Pe-type sol–gel process	XRD, FESEM, PL, CL	Luminescence	Excellent CL, good chromaticity, stability, environment friendly, $LaAlO_3:Sm^{3+}$ has potential applications in FED devices	[42]
Emulsion combustion method	DTA, TGA, FTIR, XRD, TEM	Particle size	Pure $LaAlO_3$ nano-powders (particle size = 60 nm) without intermediate phase formation	[43]
Citrate precursor technique	XRD, FTIR, TGA, DTA	Thermochemical behavior	Pure $LaAlO_3$ nanoparticles (size $\sim$30 nm)	[44]

Table 1 continued

Synthesis	Characterization	Study	Remarks	Ref.
Reverse microemulsion process	DTA, TGA, XRD, TEM	–	Spherical $LaAlO_3$ nanoparticles (size ~0 nm), this process reduces crystallization temperature (approx. 700 °C) compared with classical solid-state reaction method	[45]
Reverse micelle method	TGA, DTA, XRD, SEM, TEM, FTIR	Effect of water-to-surfactant ratio on particle size	Pure $LaAlO_3$ phase, nanoparticles, average particle size increases from 19 ± 3 to 40 ± 5.6 nm and 20.67 ± 2.07 to 32.24 ± 4.80, respectively, as the water-to-surfactant molar ratio increases from 4 to 8	[46]
Calcination of precursor (sucrose method)	XRD, DTA, TGA, QMS, BET, FESEM, TEM	Electrokinetic behavior of $LaAlO_3$	Phase pure nano-crystalline $LaAlO_3$ powder with high specific average surface area of ~43 $m^2\ g^{-1}$, average crystallite size ~30 nm, it has zero charge at approximately pH 9.9, low temperature 700–800 °C	[47]
Precipitation method	TGA, DTA, XRD, TEM, HRTEM, SAED, Raman spectra	Symmetry of $LaAlO_3$ nanocrystals as a function of crystallite size ($LaAlO_3$:Pr^{3+})	Samples with larger mean size have rhombohedral structure, which is absent in samples with smaller mean size, size ranges from few to dozens of nanometers and size increases with increasing annealing temperature	[10]
High-temperature solid-state synthesis	XRD, PL, PLE	Luminescence	Enhanced emission of green-light emission is of crucial importance in combining white light with intrinsic blue emission of Eu^{2+} and intrinsic red emission of Eu^{3+} in this mixed-valence Eu co-doped full-color phosphor	[50]
Precipitation method	XRD, TEM	Spectroscopic properties	$LaAlO_3$ nanocrystals of different average sizes ranging from 80 to 160 nm are obtained, have cubic symmetry, with increasing $LaAlO_3$ perovskite size the rhombohedral distortion increases, by controlling the size it is possible to modify the structure and thus the spectroscopic properties; $LaAlO_3$ may find application in magnetoresistance devices	[52]
Czochralski method in institute of electronic materials technology in Warsaw	–	Concentration effects on Pr^{3+} luminescence in $LaAlO_3$ crystals	Shorter non-exponential decay was observed with increasing activator concentration	[53]

Table 1 continued

Synthesis	Characterization	Study	Remarks	Ref.
Citrate precursor technique	TGA, DTA, XRD, FTIR, SEM, TEM	–	Particle sizes $\leq$100 nm, average crystallite size $\sim$24 nm, high sinterability	[56]
Pulsed laser deposition	SPA, AFM, XPS, HR-TEM	Effect of different oxygen partial pressure on $LaAlO_3$ thin film properties and resistive switching characteristics	LAO films grown at higher oxygen partial pressure provide lower leakage current, and more stable high to low resistance ratio; the interfacial layer serves as a good reservoir for oxygen ions; migration of ions between interfacial layer and LAO film may be the switching mechanism involved	[57]
Czochralski method	ESR	Effects of UV photon irradiation on transition metal impurities in $LaAlO_3$	On exposing $LaAlO_3$ to photons with energy ($\geq$4.5 eV), the intensities of ESR signals due to Cr^{3+} and Fe^{3+} decrease which indicates that electrons released by the photon irradiation are captured by Cr^{3+} and Fe^{3+}; a broad optical absorption band at approximately 3.0 eV (because of combination of a hole and a La^{3+} or Al^{3+}) and two new broad and weak ESR signals appear (assigned to the O^- center and F^+ center)	[58]
Combination of mechanically induced metathesis reaction and molten salt synthesis	XRD, TEM, Raman, IR, luminescence methods	Luminescence and phonon properties	Nano-crystalline (mean crystallite size is 50–60 nm) have $R\bar{3}c$ structure similar to that of the bulk $LaAlO_3$; low temperature synthesis (500 °C); cross-relaxation processes quench emission intensity of samples doped with Dy^{3+} and Er^{3+}	[59]
Self-combustion synthesis	XRD, TGA, DTA, SEM, TEM, EDS	–	Single phase of inverse perovskite structure of $LaAlO_3$ with crystallite size between 40 and 70 nm	[60]
Co-precipitation method	FTIR, TGA, DTA, XRD, laser diffusion	–	No reflection peaks of La_2O_3 and Al_2O_3, calcination temperature is so far the lowest process temperature for complete $LaAlO_3$ formation (700 °C), nano-crystalline size increases from 31 to 44.5 nm on increasing the calcination temperature from 700 to 1,000 °C.	[61]

Table 1 continued

Synthesis	Characterization	Study	Remarks	Ref.
Molten salt method	XRD, TGA, DTA, SEM, ED-X-ray spectrometry, WDXFS	–	Facile, rapid, simple, cost-effective, and environment-friendly (non-toxic) method, high yield, no special handling precautions, reduced synthesis time and temperature (350 °C), $LaAlO_3$ powders composed of loosely agglomerated nanoparticles with very fine crystallite size (32–45 nm), single phase samples obtained only in reactive (basic) fluxes	[62]
–	–	Structural and optoelectronic properties under pressure	With increasing external pressure, lattice constant and bond length decrease; the compound at zero pressure is an indirect band-gap semiconductor; while the indirect nature shifts to direct with increasing pressure, mixed nature of bonding (ionic and covalent)	[64]
Pulsed laser deposition method	XRD	Electrical transport property of artificial $LaNiO_3$–$LaAlO_3$ superlattice	Highly qualified crystal structure of the superlattices	[65]
Two step method-mechanically induced metathesis reaction and molten salt synthesis	XRD, TEM, HRTEM, luminescence	Optical properties	$LaAlO_3$ doped with Eu^{3+} and Er^{3+} with mean crystallite size ∼45 and ∼57 nm respectively, Eu^{3+} ions occupy three different local sites without inversion symmetry	[66]
Simple polymer complexing plus combustion method	XRD, TEM, SEM	–	–	[67]
Combustion synthesis	FTIR, XRD, SEM, TEM, fluorescence spectroscopy	Photoluminescence	Pure $LaAlO_3$ phase obtained at 800 °C, no intermediate phase, average crystal size of 60 nm, intense PL at 616 nm, material can be used as a red phosphor	[68]

EDTA ethylene diamine tetra acetic acid, *XPS* X-ray photoelectron spectroscopy, *ESR* electron spin resonance, *PLE* photoluminescence of excitation, *PA-FTIR* photoacoustic infrared spectroscopy, *XRF* X-ray fluorescence, *EDXRS* energy-dispersive X-ray spectroscopy, *SAEDP* selected area electron diffraction pattern, *HRTEM* high-resolution transmission electron microscopy, *RHEED* reflection high-energy electron diffraction, *PMMA* poly(methyl methacrylate), *PEG* polyethylene glycol, *EDS* energy-dispersive spectroscopy, *QMS* quadrupole mass spectrometer, *SPA* semiconductor parameter analyzer, *WDXFS* wavelength-dispersive X-ray fluorescence spectrometer, *FESEM* field emission scanning electron microscopy, *FTIR* Fourier-transform infrared spectroscopy, *SIMS* secondary ion mass spectroscopy

Characterization

X-ray diffraction

XRD is a technique used to measure the structural properties of a material, for example strain, epitaxy, phase composition, preferred orientation, and defect structure. XRD is non-destructive and can be used in most environments, making it advantageous over other techniques that can also be used for analysis of crystalline phases, for example TEM, which is a destructive technique. XRD can be used to determine the thickness of thin films and multilayers. It is important in many technological applications because of its ability to determine strain states. For magnetic thin films, it can be used to uniquely identify phases and preferred orientations, because these can determine magnetic properties. Figure 1 shows the XRD pattern of $LaAlO_3$ prepared by chemical coprecipitation; it shows that the calcined $LaAlO_3$ precursor powders are representative of $LaAlO_3$, and no reflections from La_2O_3 and Al_2O_3 are observed as distinct intermediate phases during formation of $LaAlO_3$ by thermal decomposition of the precursor powders, even at 1,000 °C [61] (Fig. 2).

TGA and DTA

TGA involves measurement of the weight of a sample under investigation as the temperature is increased at a pre-determined rate. The sample may either lose weight to the atmosphere or gain weight by reaction with the atmosphere. The TGA record is generally in the form of an integral curve, with absolute weight (*W*) as the *Y* axis and time (*t*) or temperature (*T*) as the *X* axis. The shape of the thermogravimetric curve is affected by several factors, the most important being heating rate, sample, and atmosphere.

DTA is measurement of the difference in temperature between a sample and a reference as heat is applied to the system. It is a fingerprint technique which provides information about the chemical reactions, phase transformations, and structural changes that occur in a sample during a heating or cooling cycle. The

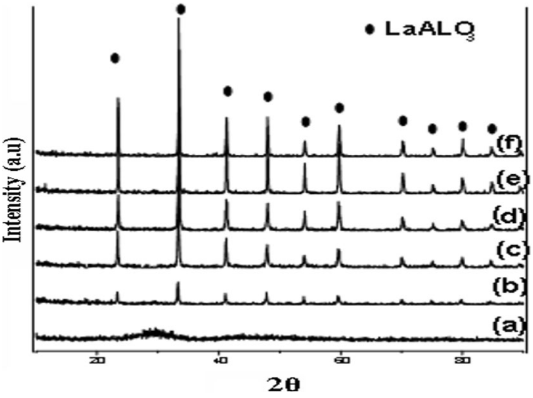

Fig. 1 XRD patterns of the $LaAlO_3$ precursor powders calcined at different temperatures for 6 h: (*a*) 500 °C, (*b*) 600 °C, (*c*) 700 °C, (*d*) 800 °C, (*e*) 900 °C, and (*f*) 1,000 °C [61]

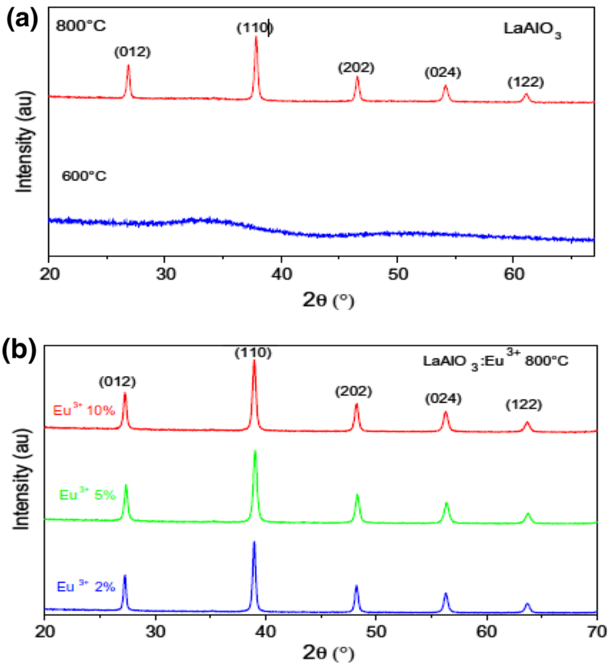

Fig. 2 XRD patterns of $LaAlO_3$:Eu^{3+} **a** temperature variation and **b** doping concentration variation [68]

DTA technique is especially suited to studies of structural changes within a solid at elevated temperatures, where few other methods are available. TGA and DSC curves of the hydroxide precursor of $LaAlO_3$ (prepared by the reverse microemulsion process) are shown in Fig. 3. TGA and DSC were performed at a heating rate of 10 °/min under static air on SDT Q600 instruments. The DSC curve indicates the presence of one exothermic peak at 479 °C and two endothermic peaks at 46 and 315 °C, respectively. The endothermic peak at 46 °C corresponds to elimination of residual water and solvent. The endothermic peak at 315 °C represents the decomposition of $Al(OH)_3$ and $La(OH)_3$. The exothermic peak at 479 °C may be associated with combustion of the residual surfactant or cosurfactant. The TGA curve is in agreement with DSC peaks and shows distinct weight-loss in regions corresponding to the temperature regions in DSC.

FTIR spectroscopy

FTIR spectroscopy is rapidly becoming a common feature in modern spectroscopy laboratories. The Fourier-transform technique depends upon the basic principle that any wave function can be represented as a series of sine and cosine functions with different frequencies. IR analysis of synthesized samples is important for control both of the reaction process and of the properties of the materials obtained. The FTIR absorption spectra of $LaAlO_3$ precursor powders calcined at different temperatures for 6 h are shown in Figs. 4 and 5.

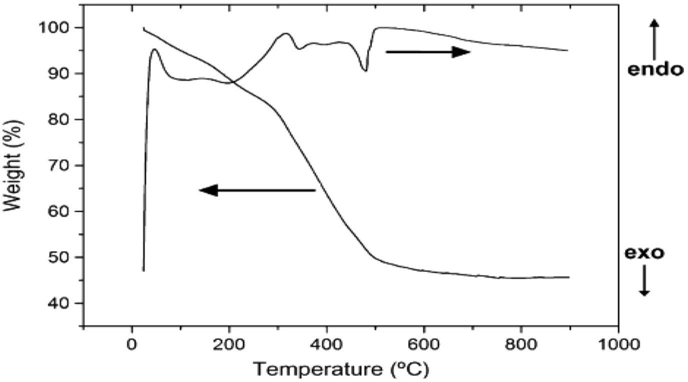

Fig. 3 TGA–DSC curves of the hydroxide precursor [45]

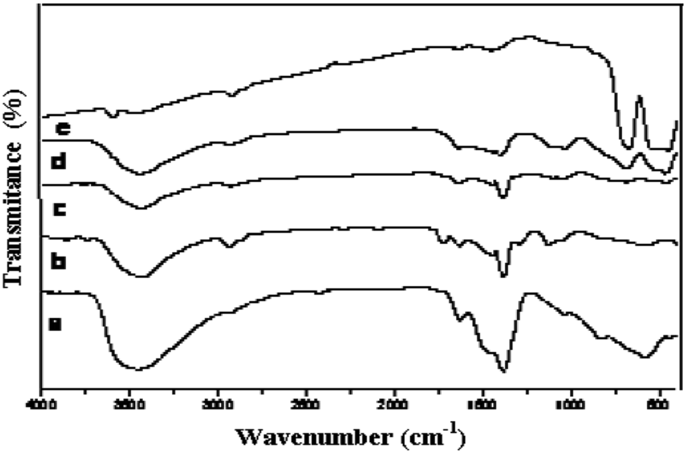

Fig. 4 FTIR absorption spectra of $LaAlO_3$ precursor powders calcined at different temperatures for 6 h: (*a*) room temperature, (*b*) 200 °C, (*c*) 500 °C, (*d*) 600 °C, (*e*) 700 °C [61]

Transmission electron microscopy

Historically, TEM has been a complementary tool for X-ray structural crystallographers owing to the insufficient image resolution at the time (which has since been overcome) and in the poor quality of diffraction data, as a consequence of multiple (dynamic) scattering. Today however, the electron microscope has the advantage of being able to form a fine probe for nano-scale characterization while simultaneously enabling collection of improved diffraction patterns with kinematic or near-kinematic data. TEM enables a variety of experiments for characterization of materials, not only to determine the properties of the bulk materials but also to obtain surface information. For example, surface morphology, surface unit cell dimensions, surface atomic positions, and even surface charge density and charge transfer can be observed. TEM micrographs of $LaAlO_3$ powder calcined at 800 °C

Fig. 5 IR spectra of the $LaAlO_3$ system prepared by the 2.5 PVA method. (*a*) Precursor powder, and after calcination of the precursor powder for 2 h at (*b*) 500 °C, (*c*) 700 °C, and (*d*) 800 °C [4]

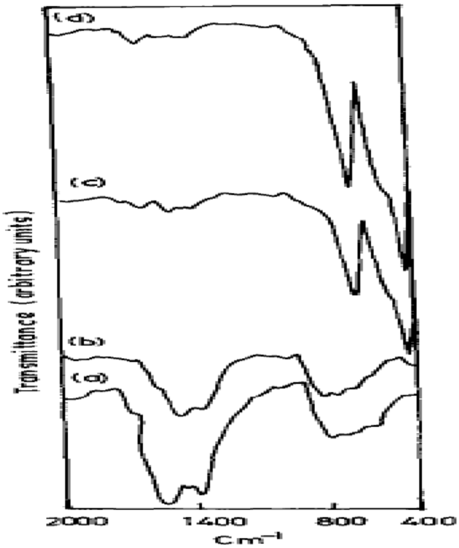

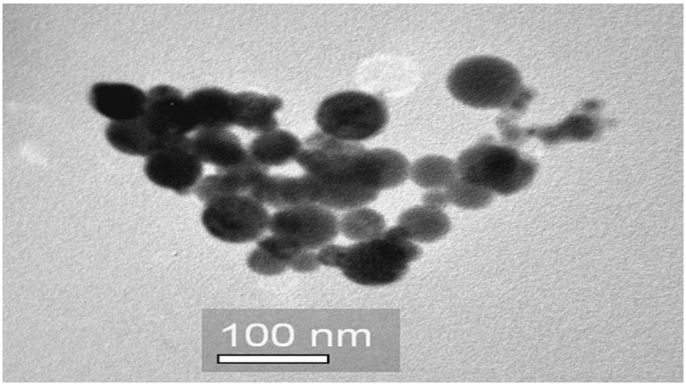

Fig. 6 TEM micrograph of $LaAlO_3$ particles calcined at 800 °C for 2 h [45]

are shown in Fig. 6. From the TEM images it can be seen that individual particles are spherical in shape, with particle size of approximately 50 nm, and are loosely agglomerated.

Scanning electron microscopy

An SEM obtains topographic images of organic and inorganic materials and enables elemental analysis. Its usefulness stems from its capability of obtaining 3D-like images of the surfaces of different samples and specimens. Most elements can be identified by use of the electron dispersive spectrometer portion of the SEM. The

SEM's instrumental resolution is generally approximately 10–50 Å; it also has a large depth of field, which is responsible for the 3D appearances of sample imaging. Overall the SEM's most important use is for structural analysis and elemental analysis. An SEM micrograph of powder calcined at 700 °C is shown in Fig. 7. The synthesized powder is partially agglomerated and its particle size is smaller than 100 nm. The rough surface indicates that these particles are essentially secondary agglomerates of finer particles.

Photoluminescence

Photoluminescence (abbreviated "PL") is a process in which a substance absorbs photons (electromagnetic radiation), hence the prefix "photo", and then re-radiates photons. Quantum mechanically, this can be described as excitation to a higher energy state and then a return to a lower energy state accompanied by emission of a photon. This is one of many forms of luminescence (light emission). The period between absorption and emission is typically extremely short, of the order of 10 ns. In special circumstances, however, this period can be extended to minutes or hours. The normalized PL spectra of single (Eu^{3+}) and co-doped (Eu^{2+}, Eu^{3+}) samples on excitation with UV light are presented in Fig. 8a, b, respectively. The inset in Fig. 8a shows the partial PL spectral range from 380 to 560 nm for the single-doped sample. It is found that strong red emission at ~592 and ~618 nm and several sub-emission peaks located in the blue–green region are observed for the single-doped sample. The emission intensity of sub-emission peaks is so weak it can be neglective compared with the strong red emission, as shown in Fig. 8a. Full color emission is recorded for the mixed-valence Eu co-doped sample, as shown in Fig. 8b. The red emission arises from the same transitions as for the above Eu^{3+} single-doped sample whereas the blue emission band at approximately 445 nm is assigned to the transition emission of Eu^{2+}. In addition, emission of green light at 515 nm is clearly apparent in the PL spectrum of the co-doped sample.

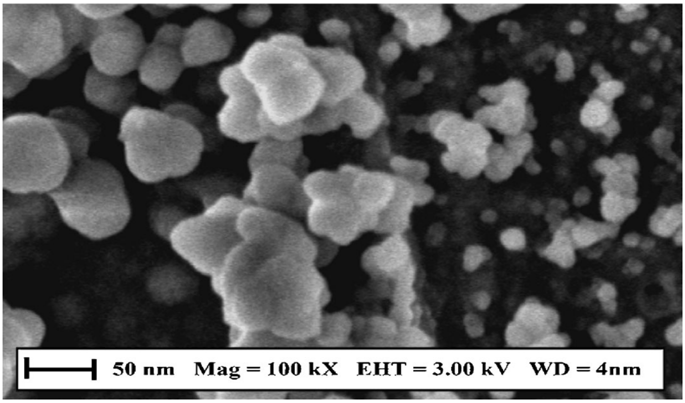

Fig. 7 FESEM micrograph of the calcined $LaAlO_3$ powder at 700 °C for 1 h [47]

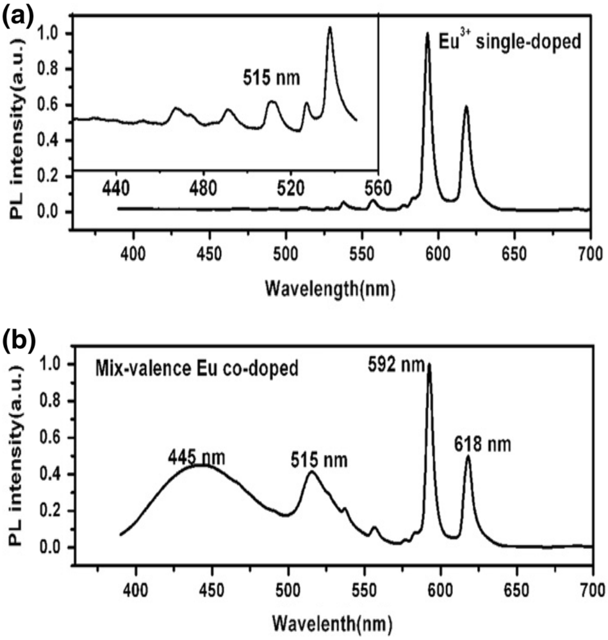

Fig. 8 Normal PL spectra of **a** Eu^{3+} single-doped and **b** mixed-valence Eu co-doped samples on excitation of UV light. The *inset* is the partial PL range from 380 to 560 nm for the Eu^{3+} single-doped sample [50]

Atomic force microscopy

AFM or scanning force microscopy is a very high-resolution type of scanning probe microscopy, with demonstrated resolution of the order of fractions of a nanometer, more than 1,000 times better than the optical diffraction limit. The precursor to the AFM, the scanning tunneling microscope, was developed by Gerd Binnig and Heinrich Rohrer in the early 1980s at IBM Research, Zurich, a development that earned them the Nobel Prize for Physics in 1986. Binnig, Quate, and Gerber invented the first atomic force microscope (also abbreviated as AFM) in 1986. The first commercially available AFM was introduced in 1989. The AFM is one of the foremost tools for imaging, measurement, and manipulation of matter on the nanoscale. The information is gathered by "feeling" the surface with a mechanical probe. Piezoelectric elements that facilitate tiny but accurate and precise movements on (electronic) command enable very precise scanning. In some variations, electric potentials can also be scanned by use of conducting cantilevers. In more advanced versions, currents can be passed through the tip to probe the electrical conductivity or transport of the underlying surface, but this is much more challenging with few research groups reporting consistent data. Figure 9 shows the 3D AFM image of an LAO–SrO–Si sample. The surface of the LAO film is atomically smooth, and no particles or islands have been found.

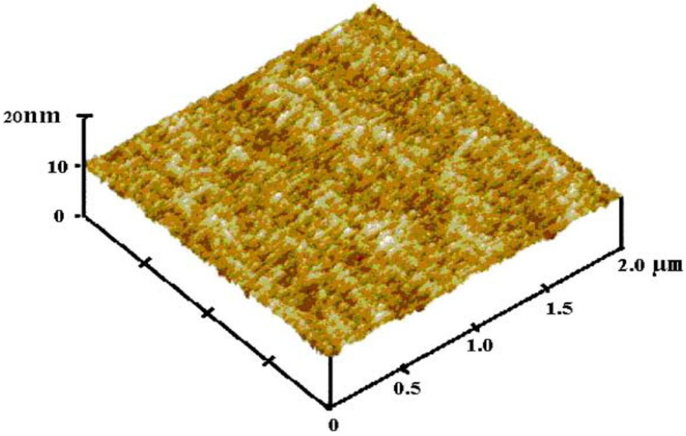

Fig. 9 3D AFM image of LAO thin film for determination of LAO–SrO–Si structure [21]

Electrokinetic behavior

The electrokinetic behavior of nano-sized $LaAlO_3$ powder calcined at 800 °C is depicted in Fig. 10. It has a pzc at approximately pH 9.9. It is obvious from the zeta-potential curve that the surface charge of the $LaAlO_3$ particles dispersed in an aqueous solvent depends on the pH of the suspension. At low pH $LaAlO_3$ is positively charged and at pH above pzc it is negatively charged.

Dielectric behavior

Figure 11 below shows the dielectric behavior of $LaAlO_3$ as a function of temperature (from room temperature to 300 °C). A strong dielectric assembly was found at 66 °C. The dielectric constant (ε) increases sharply from room temperature to its maximum value of 35 at 66 °C and then decreases gradually to 180 °C and

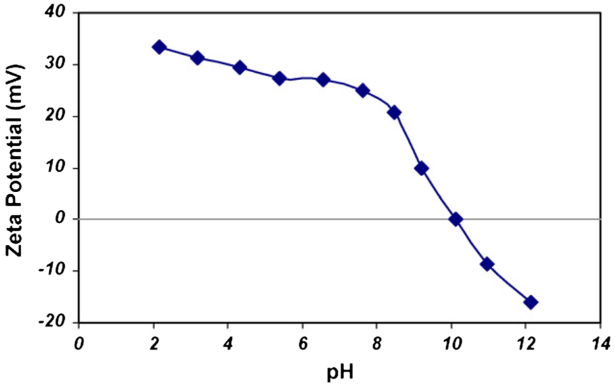

Fig. 10 Potential behavior of the synthesized nano-crystalline $LaAlO_3$ at 800 °C in 1 M KCl solution (solid portion of suspension = 6 % *w*/*w*) [47]

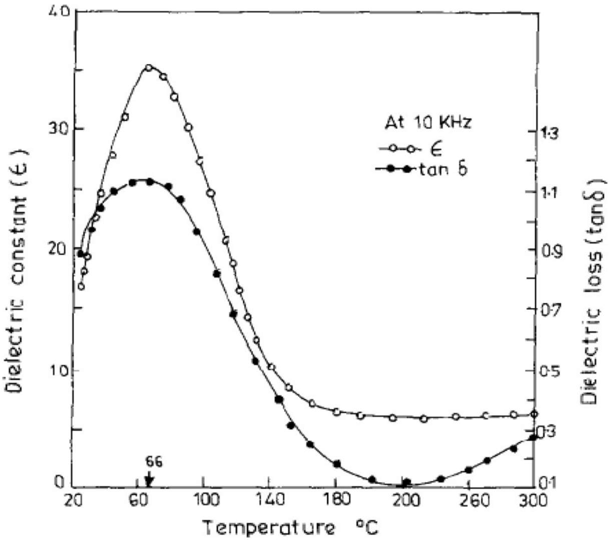

Fig. 11 Variation of dielectric constant (ε) and dielectric loss (tan δ) as a function of temperature at 10 kHz [4]

ultimately becomes constant at approximately 6. The room temperature dielectric constant was strongly supported by the reported value. The dielectric loss (tan δ), which is related to the complex part of the dielectric constant, has a diffuse peak at the same temperature and has a loss of 1.13, which indicates that conduction of the carriers was performed at that temperature. At higher temperature (>260 °C), the mode of loss increases, which is because of the space charge effect.

Perovskite crystal structure

The perovskite crystal structure is shown in Fig. 12.

Discussion

Many methods of preparation of $LaAlO_3$ nano-phosphors have been reported in this review. Although conventional solid-state reaction is a very simple method for synthesis of $LaAlO_3$, this process is not entirely satisfactory because of several serious drawbacks, for example introduction of impurities during milling, high reaction temperature, limit of complete oxide reaction and chemical homogeneity, large particle size, and low sintering ability. Extensive research has therefore been performed to prepare finer and more homogeneous powders at lower temperatures by use of a variety of chemical processes. Methods with lower synthesis temperature are preferred as they lead to a high-surface-area material, i.e. material with improved catalytic activity. Pure $LaAlO_3$ phase with average crystallite size of ~60 nm can be obtained by combustion synthesis, in which the temperature of

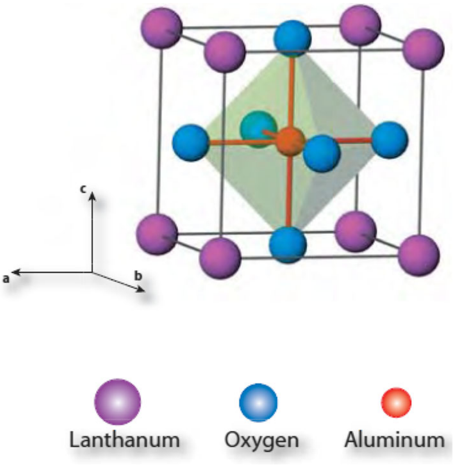

Fig. 12 The ideal ABX_3 cubic perovskite structure illustrating the octahedral coordination of the B-site (aluminium here) cations (for $LaAlO_3$) [70]

synthesis is reduced to 800 °C [29, 60, 68]. From Table 1 it is apparent that chemical coprecipitation using aqueous NH_3 as a basic precipitant is a simple method for synthesis of nano-powders of pure perovskite $LaAlO_3$. The calcination temperature (700 °C) is, so far, the lowest process temperature used for complete $LaAlO_3$ formation; nano-crystallite size increases from 31 to 44.5 nm with increasing calcination temperature from 700 to 1,000 °C [61]. Synthesis time and/or temperature are reduced in the molten salt method also (350 °C) and particle size is less than 100 nm; this technique has the advantages of being a facile, rapid, simple, cost-effective, environment-friendly, and high yielding method with no special handling precautions required. $LaAlO_3$ powders of loosely agglomerated nanoparticles with very fine crystallite size (32–45 nm) are obtained in this method [62]. For $LaAlO_3$ prepared by such methods as emulsion combustion, reverse microemulsion, and the citrate precursor technique, or by combination of mechanically induced metathesis with molten salt synthesis, average crystallite size is 50–60 nm [43, 45, 56, 59]. The combined gel precipitation process yields $LaAlO_3$ powders with fairly spherical morphology and size ~25 nm [32]. Pure single-phase nano-crystalline $LaAlO_3$ powder with a high specific average surface area of ~43 $m^2\ g^{-1}$ and average crystallite size ~30 nm can be prepared by the sucrose method [47].

Irrespective of the method chosen for preparation of $LaAlO_3$ phosphors, XRD shows that no intermediate Al_2O_3 or La_2O_3 phase is present. Pure $LaAlO_3$ has a rhombohedral structure and occurs as a single phase. Sometimes a hexagonal structure [29] is also observed, and some samples have an orthorhombic [15] or cubic structure [21]. $LaAlO_3$ doped with transition metal impurities has luminescence properties.

Pure nano-crystalline $LaAlO_3$ powders prepared by combustion synthesis using a concentrated solution of nitrates of lanthanum and aluminate as oxidizer, and glycine acid as fuel have a hexagonal structure. Particle size is 78 nm and surface area is 11 $m^2\ g^{-1}$. TEM micrography shows that the powder obtained has faceted polyhedral morphology. Samples sintered at 1,500 °C have the best microwave dielectric properties (permittivity, ε_r, = 23 and quality factor, Q_f, = 38,000 GHz). Figure 14 shows ε_r and Q_f as a function of sintering temperature [29] (Fig. 13).

$LaAlO_3$ films grown on Si by laser molecular beam epitaxy have a single cubic crystalline structure. The surface of the epitaxial $LaAlO_3$ films were atomically smooth. Figure 10 shows the 3D AFM image of a thin film of LAO–SrO–Si. This successful growth of $LaAlO_3$ on Si suggests the possibility of development of 3D heterostructures on Si in a new generation of microelectronics devices [21]. $LaAlO_3$ with an orthorhombic structure has also been prepared by homogeneous precipitation from aqueous solutions containing urea [15].

$LaAlO_3$ has excellent chemical and thermal stability (mp ~2,110 °C), mechanical durability, and exploitable optical and electrical properties, leading to a wide range of potential applications. $LaAlO_3$ has an excellent lattice match and good thermal expansion matching with many materials with the perovskite structure and, hence, is frequently used as a substrate and buffer layer for deposition of high-temperature superconductor and ferroelectric thin films. Because of its elegant dielectric properties, and high quality factor (Q_f) and relative permittivity (ε_r), $LaAlO_3$ is also a promising candidate for low-loss microwave and dielectric resonance applications; $LaAlO_3$ is, thus, widely used in superconducting microwave devices. Experimental work also demonstrates that $LaAlO_3$ is a potential candidate for SiO_2 replacement because of its high k value. At elevated temperature $LaAlO_3$ has the cubic perovskite structure but transforms into a trigonal rhombohedral form at approximately 800 K. The capabilities of perovskite oxide materials just as remarkable dielectric, piezoelectric, ferroelectric, optical, electro-optic, ferromagnetic, superconducting and catalytic properties have close relation with the energy spectrum. It has been also used as a support for combustion catalysts or even as a catalyst itself for oxidative coupling of methane and hydrogenation of hydrocarbons. Finally, with La^{3+} and/or Al^{3+} partially replaced by Sr^{2+} and/or Mg^{2+}, respectively, it becomes a good oxygen ion-conducting material at low oxygen partial pressures and high temperatures, changing to a mixed ionic and p-type electronic conductor at high oxygen pressures. Phosphors are important materials in modern

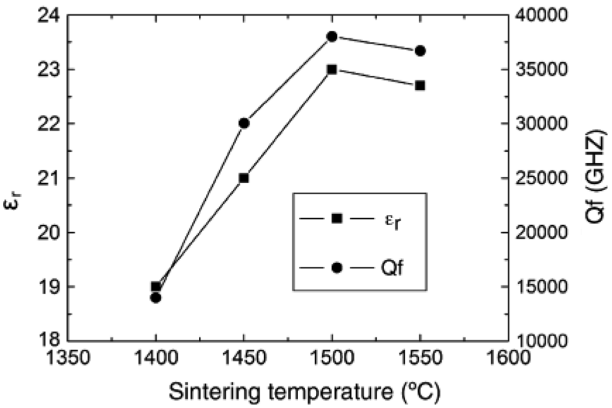

Fig. 13 Microwave dielectric properties of $LaAlO_3$ ceramics sintered at different temperature [29]

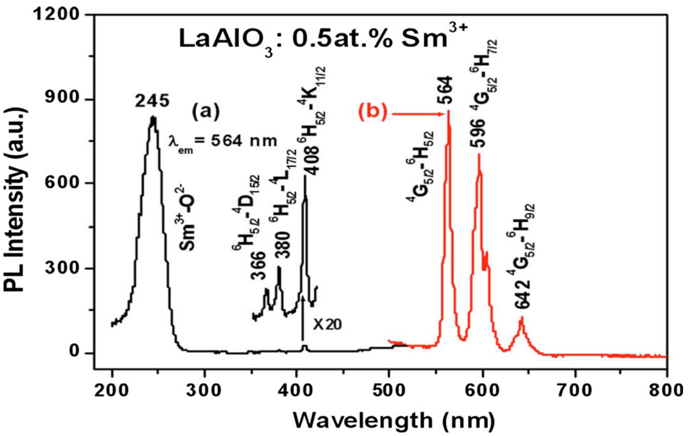

Fig. 14 Color online excitation (*a*) and emission (*b*) spectra of LaAlO$_3$:0.5 at.% Sm^{3+} annealed at 800 °C [42]

technology because of their ability to convert incident electromagnetic radiation into light.

Rare-earth (RE) ions have been widely used as activators in different host matrices because of their highly efficient emission performance. The development of RE-ion-doped novel luminescent phosphors is therefore of interest because of their potential applications in different optical display systems. LaAlO$_3$ has been chosen as a host material because it has a reasonably large band gap of >5 eV and high thermal stability up to 2,100 °C. RE-doped LaAlO$_3$ also has remarkable properties which can be exploited, for example, to enhance solar efficiency, laser action, etc.

LaAlO$_3$:Sm^{3+} phosphors have been prepared by a Pe-type sol–gel process. On excitation with UV light or low-voltage electron beams, the phosphors emit yellow luminescence with good chromaticity coordinates (Fig. 14). The CL properties of LaAlO$_3$:Sm^{3+} are, to some extent, comparable with those of the corresponding commercial low-voltage phosphors. Because of their excellent CL, good CIE chromaticity, stability, and environmentally friendly properties, LaAlO$_3$:Sm^{3+} phosphors have potential applications in FED devices [42]. Dy^{3+} in the LaAlO$_3$ host lattice emits light from the blue to red region. The most intense is yellow–greenish emission (Figs. 15, 16). The emission of LaAlO$_3$:Er^{3+} is weaker than that of LaAlO$_3$:Dy^{3+} [59]. Eu^{3+}-doped LaAlO$_3$ nano-phosphors are prepared by combustion synthesis. Typically the Eu^{3+} ion emits characteristic red light with a number of narrow lines. The PL emission intensity increases when the Eu^{3+} concentration is increased from 2 %, reaching a maximum when the concentration of Eu^{3+} is 5 % and then decreasing slightly for higher concentrations (Figs. 17, 18) [68].

Conclusion

From the discussion above we conclude that the combustion, chemical coprecipitation, sucrose, and molten salt methods are best for low-temperature synthesis of

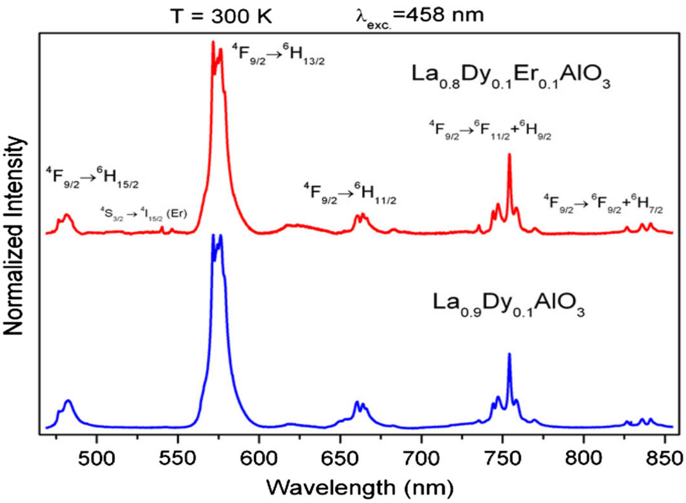

Fig. 15 Emission spectra of $La_{0.9}Dy_{0.1}AlO_3$ and $La_{0.8}Dy_{0.1}Er_{0.1}AlO_3$ [59]

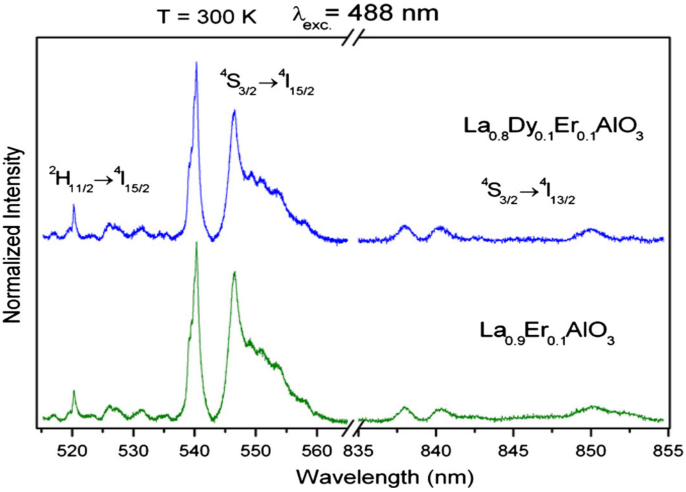

Fig. 16 Emission spectra of $La_{0.9}Er_{0.1}AlO_3$ and $La_{0.8}Dy_{0.1}Er_{0.1}AlO_3$ [59]

$LaAlO_3$ phosphors. $LaAlO_3$ prepared by use of the combustion method is reported to have the best microwave properties. Among all the methods used to prepare $LaAlO_3$ nano-crystalline phosphors, only methods which give single-phase pure perovskite $LaAlO_3$ of small particle size, small average crystallite size, and high specific surface area are preferred. The rhombohedral structure of $LaAlO_3$ has been reported most often. Orthorhombic, hexagonal, and cubic structures are occasionally reported. $LaAlO_3$ has exploitable optical and electrical properties and is widely used in superconducting microwave devices. RE-doped-$LaAlO_3$ has potential applications in optical display systems. $LaAlO_3$ doped with transition elements emits

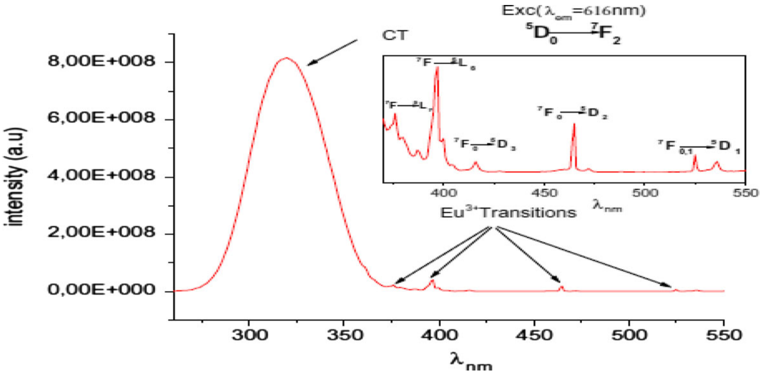

Fig. 17 Excitation spectra of $LaAlO_3$:Eu (5 %) [68]

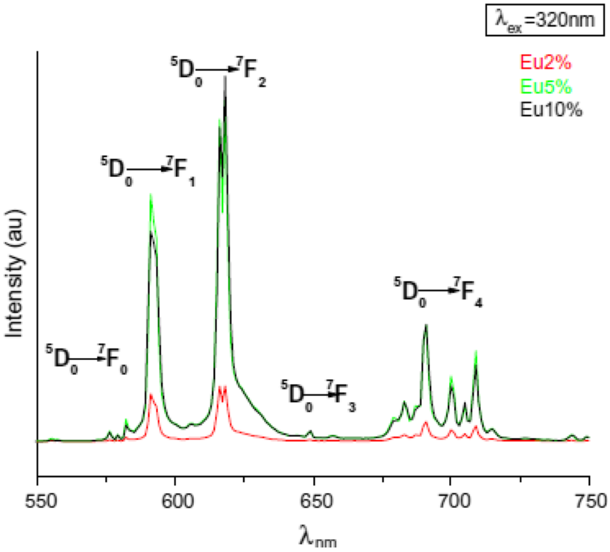

Fig. 18 Emission spectra of $LaAlO_3$:Eu (2 %, 5 %, 10 %) obtained at 800 °C [68]

luminescence, as discussed in detail above. These RE ions act as activators in $LaAlO_3$ phosphors. The chemical and thermal stability and mechanical durability of $LaAlO_3$ phosphors are excellent, and their exploitable optical and electronic properties lead to a wide range of potential applications.

References

1. R.K. Simon, C.E. Platt, K.P. Daly, A.E. Lee, M.K. Wager, Appl. Phys. Lett. **53**, 2677 (1988)
2. B. Jancar, D. Suvorov, M. Valant, G. Drazic, J. Eur. Ceram. Soc. **23**, 1391 (2003)
3. I. Zvereva, Y. Smirnov, V. Gusarov, V. Popova, J. Choisnet, Solid State Sci. **5**, 343 (2003)

4. A.K. Adak, P. Pramanik, Mater. Lett. **30**, 269 (1997)
5. M. Chroma, J. Pinkas, I. Pakutinskiene, A. Begankiene, A. Kareiva, Ceram. Int. **31**, 1123 (2005)
6. S.N. Koc, F. Oksuzomer, E. Yasav, S. Akturk, M.A. Gurkaynak, Mater. Res. Bull. **41**, 2291 (2006)
7. A. Barrera, S. Fuentes, M. Viniegra, M. Avalos-Borja, N. Bogdan Chikova, J.C. Molina, Mater. Res. Bull. **42**, 640 (2007)
8. Y. Xu, G. Huang, H. Long, Ceram. Int. **29**, 837 (2003)
9. D. Zhou, G. Huang, X. Chen, J. Xu, S. Gong, Mater. Chem. Phys. **84**, 33 (2004)
10. P.J. Deren, K. Lemanski, A. Gagor, M. Watras, M. Malecka, M. Zawadzki, J. Solid State Chem. **183**, 2095 (2010)
11. R. Pazik, G.A. Seisenbaeva, R.J. Wiglusz, L. Kepinski, V.G. Kessler, Inorg. Chem. **50**, 2966 (2011)
12. S. Ran, L. Gao, Ceram. Int. **34**, 443 (2008)
13. J.J. Kingsley, K.C. Patil, Mater. Lett. **6**, 427 (1988)
14. M.D. Shaji Kumar, T.M. Srinivasan, P. Ramasamy, C. Subramanian, Mater. Lett. **25**, 171 (1995)
15. E. Taspinar, A. Cuneyt Tas, J. Am. Ceram. Soc. **80**(1), 133 (1997)
16. J.P. Jacobs, M.A.S. Miguel, L.J. Alvarez, J. Mol. Struct. (Theochem) **390**, 193 (1997)
17. M. Kakihana, T. Okubo, J. Alloys Compd. **266**, 129 (1998)
18. R. Spinicci, P. Marini, S. De Rossi, M. Faticanti, P. Porta, J. Mol. Catal. A **176**, 253 (2001)
19. S.A. Hayward, S.A.T. Redfern, E.K.H. Salje, J. Phys. Condens. Matter **14**, 10131 (2002)
20. P.J. Deren, J.C. Krupa, J. Lumin. **102**, 386 (2003)
21. W.F. Xianga, H.B. Lua, Z.H. Chena, X.B. Lub, M. Hea, H. Tiana, Y.L. Zhoua, C.R. Lia, X.L. Mac, J. Cryst. Growth **271**, 165 (2004)
22. P.J. Deren, J.C. Krupa, J. Alloys Compd. **380**, 362 (2004)
23. E.A. Fidancev, P.J. Deren, J.C. Krupa, J. Alloys Compd. **380**, 376 (2004)
24. T. Busani, R.A.B. Devine, J. Appl. Phys. **96**, 6642 (2004)
25. C. Chang, Z. Yuan, D. Mao, J. Alloys Compd. **415**, 220 (2006)
26. D. Hreniak, W. Strek, P. Deren, A. Bednarkiewicz, A. Lukowiak, J. Alloys Compd. **408**, 828 (2006)
27. P. Deren, Ph. Goldner, O.G. Noel, J. Lumin. **119**, 38 (2006)
28. T. Ishigaki, K. Seki, E. Nishimura, T. Watanabe, M. Yoshimura, J. Alloys Compd. **408**, 1177 (2006)
29. Z.Q. Tian, H.T. Yu, Z.L. Wang, Mater. Chem. Phys. **106**, 126 (2007)
30. C.L. Kuo, C.L. Wang, T.Y. Chena, G.J. Chenb, I.M. Hung, C.J. Shih, K.Z. Funga, J. Alloys Compd. **440**, 367 (2007)
31. Z. Li, S. Zhang, W.E. Lee, J. Eur. Ceram. Soc. **27**, 3201 (2007)
32. S.K. Behera, P.K. Sahu, S.K. Pratihar, S. Bhattacharyya, J. Phys. Chem. Solids **69**, 2041 (2008)
33. X. Luo, B. Wang, J. Appl. Phys. **104**, 073518 (2008)
34. P.J. Deren, Ph. Goldner, O.G. Noel, J. Alloys Compd. **461**, 58–60 (2008)
35. X. Luo, B. Wang, J. Appl. Phys. **104**, 053503 (2008)
36. V. Singh, D.T. Naidu, R.P.S. Chakradhar, Y.C. Ratnakaramd, J.J. Zhu, M. Soni, Physica B **403**, 3781 (2008)
37. P.J. Dereń, A. Bednarkiewicz, Ph. Goldner, O. Guillot-Noël, J. Appl. Phys. **103**, 043102 (2008)
38. A. Gocalinska, P.J. Deren, P. Głuchowski, Ph. Goldner, O. Guillot-Noel, Opt. Mater. **30**, 680 (2008)
39. T. Kharlamova, S. Pavlova, V. Sadykov, O. Lapina, D. Khabibulin, T. Krieger, V. Zaikovskii, A. Ishchenko, A. Salanov, V. Muzykantov, N. Mezentseva, M. Chaikina, N. Uvarov, J. Frade, Chr. Argirusis, Solid State Ion. **179**, 1018 (2008)
40. P.J. Deren, R. Mahiou, Ph. Goldner, Opt. Mater. **31**, 465 (2009)
41. I.Y.K. Chang, S.W. You, M.G. Chen, P.C. Juan, C.H. Chen, J.Y. Lee, J. Appl. Phys. **105**, 104512 (2009)
42. X. Liu, J. Zou, J. Lin, J. Electrochem. Soc. **156**(2), P43 (2009)
43. J. Chandradass, K.H. Kim, J. Alloys Compd. **481**, L31 (2009)
44. H.F. Yu, J. Wang, S.S. Wang, Y.M. Kuo, J. Phys. Chem. Solids **70**, 218 (2009)
45. Z. Tian, W. Huang, Y. Liang, Ceram. Int. **35**, 661 (2009)
46. J. Chandradass, H.K. Kim, J. Cryst. Growth **311**, 3631 (2009)
47. Z. Negahdaria, A. Saberi, M.W. Poradaa, J. Alloys Compd. **485**, 367 (2009)
48. A. Boudali, B. Amrani, M.D. Khodja, A. Abada, K. Amara, Comput. Mater. Sci. **45**, 1068 (2009)
49. P. Zhang, J.-P. Zhanga, Eur. Phys. J. B **78**, 1 (2010)
50. Z.Y. Mao, Y.C. Zhu, Q. Fei, D. Wang, J. Lumin. **131**, 1048 (2011)
51. B. Liu, F. Yuan, X. Huc, J. Phys. Chem. Solids **72**, 380 (2011)
52. P.J. Deren, K. Lemanski, J. Lumin. **131**, 445 (2011)
53. M. Malinowski, M. Kaczka, S. Turczynski, D. Pawlak, Opt. Mater. **33**, 1004 (2011)

54. H. Mortada, D. Dentel, M. Derivaz, J.L. Bischoff, E. Denys, R. Moubah, C.U. Bouillet, J. Werckmann, J. Cryst. Growth **323**, 247 (2011)
55. M. Dudek, A. Jusza, K. Anders, L. Lipinska, M. Baran, R. Piramidowicz, J. Rare Earths **29**(12), 1123 (2011)
56. H.F. Yu, Y.M. Guo, J. Alloys Compd. **509**, 1984 (2011)
57. K.C. Liu, W.H. Tzeng, K.M. Chang, J.J. Huang, Y.J. Lee, P.H. Yeh, P.S. Chen, H.Y. Lee, F. Chen, M.J. Tsai, Thin Solid Films **520**, 1246 (2011)
58. D. Yamasaka, K. Tamagawa, Y. Ohki, J. Appl. Phys. **110**, 074103 (2011)
59. M. Maczka, E.M. Mendoza, A.F. Fuentes, K. Lemanski, P. Deren, J. Solid State Chem. **187**, 249 (2012)
60. K.A. Khamkar, S.V. Bangale, S.R. Bamane, V.V. Dhapte, Der Chem. Sin. **3**(4), 891 (2012)
61. L. Djoudi, M. Omari, N. Madoui, EPJ. Web Conf. **29**, 16 (2012)
62. E.M. Mendoza, S.M. Montemayor, J.I.E. Garcı, A.F. Fuentes, J. Am. Ceram. Soc. **95**(4), 1276 (2012)
63. H. Li, J. Robertson, J. Appl. Phys. **112**, 034108 (2012)
64. G. Murtaza, I. Ahmad, J. Appl. Phys. **111**, 123116 (2012)
65. A.N. Jang, S.K. Seung, K.H. Choi, J.H. Song, Ceram. Int. **38S**, S627 (2012)
66. M. Maczka, A. Bednarkiewicz, E.M. Mendoza, A.F. Fuentes, L. Kepinski, J. Solid State Chem. **194**, 264 (2012)
67. S. Li, B. Bergman, Z. Zhao, Mater. Chem. Phys. **132**, 309 (2012)
68. A. Dhahri, K.H. Naifer, A. Benedetti, F. Enrichi, M. Ferid, Opt. Mater. **34**, 1742 (2012)
69. A. Watras, R. Pazik, P.J. Deren, J. Lumin. **133**, 35 (2013)
70. J.M. Rondinelli, *Model Catalytic Oxide Surfaces: A Study of the* $LaAlO_3$ *(001) Surface* (Northwestern University, Evanston, 2006)